

# An Unstructured Grid, Finite-Volume, Three-Dimensional, Primitive Equations Ocean Model: Application to Coastal Ocean and Estuaries

CHANGSHENG CHEN AND HEDONG LIU

*School for Marine Science and Technology, University of Massachusetts–Dartmouth, New Bedford, Massachusetts*

ROBERT C. BEARDSLEY

*Department of Physical Oceanography, Woods Hole Oceanographic Institution, Woods Hole, Massachusetts*

(Manuscript received 18 January 2001, in final form 27 June 2002)

## ABSTRACT

An unstructured grid, finite-volume, three-dimensional (3D) primitive equation ocean model has been developed for the study of coastal oceanic and estuarine circulation. The model consists of momentum, continuity, temperature, salinity, and density equations and is closed physically and mathematically using the Mellor and Yamada level-2.5 turbulent closure submodel. The irregular bottom slope is represented using a  $\sigma$ -coordinate transformation, and the horizontal grids comprise unstructured triangular cells. The finite-volume method (FVM) used in this model combines the advantages of a finite-element method (FEM) for geometric flexibility and a finite-difference method (FDM) for simple discrete computation. Currents, temperature, and salinity in the model are computed in the integral form of the equations, which provides a better representation of the conservative laws for mass, momentum, and heat in the coastal region with complex geometry. The model was applied to the Bohai Sea, a semienclosed coastal ocean, and the Satilla River, a Georgia estuary characterized by numerous tidal creeks and inlets. Compared with the results obtained from the finite-difference model (ECOM-si), the new model produces a better simulation of tidal elevations and residual currents, especially around islands and tidal creeks. Given the same initial distribution of temperature in the Bohai Sea, the FVCOM and ECOM-si models show similar distributions of temperature and stratified tidal rectified flow in the interior region away from the coast and islands, but FVCOM appears to provide a better simulation of temperature and currents around the islands, barriers, and inlets with complex topography.

## 1. Introduction

Most of the world oceans' inner shelves and estuaries are characterized by a series of barrier island complexes, inlets, and extensive intertidal salt marshes. Such an irregular geometric ocean–estuarine system presents a challenge for oceanographers involved in model development even though the governing equations of oceanic circulation are well defined and numerically solvable in terms of discrete mathematics. Two numerical methods have been widely used in ocean models: 1) the finite-difference method (Blumberg and Mellor 1987; Haidvogel et al. 1991; Blumberg 1994) and 2) the finite-element method (Lynch and Naimie 1993; Naimie 1996). The finite-difference method is the simplest discrete scheme with an advantage of computational efficiency. Introducing an orthogonal or nonorthogonal curvilinear coordinate transformation into a finite-differ-

ence model can provide a moderate fitting of coastal boundaries, but these transformations are incapable of resolving the highly irregular estuarine geometries characteristic of numerous barrier island and tidal creek complexes (Blumberg 1994; Chen et al. 2001; Chen et al. 2002, manuscript submitted to *J. Great Lakes Res.*). The greatest advantage of the finite-element method is its geometric flexibility. Triangular meshes at an arbitrary size are used in this method and can provide an accurate fitting of the irregular coastal boundary. The P-type finite-element method (Maday and Patera 1989) or discontinuous Galerkin method (Reed and Hill 1973; Cockburn et al. 1990) has been introduced into the updated finite-element model to help improve computational accuracy and efficiency.

Recently, the finite-volume method has received considerable attention in the numerical computation of fluid dynamics (Dick 1994). The dynamics of oceanography comply with conservation laws. The governing equations of oceanic motion and water masses are expressed by the conservation of momentum, mass, and energy in a unit volume. When the equations are solved numerically, these laws cannot always be guaranteed, espe-

---

*Corresponding author address:* Dr. Changsheng Chen, School for Marine Science and Technology, University of Massachusetts–Dartmouth, 706 South Rodney French Blvd., New Bedford, MA 02744-1221.  
E-mail: c1chen@umassd.edu

cially in situations with sharp thermoclines or discontinuous flow. Unlike the differential form, the finite-volume method discretizes the integral form of the equations, making it easier to comply with the conservation laws. Since these integral equations can be solved numerically by the flux calculation used in the finite-difference method over an arbitrarily sized triangular mesh (like those in a finite-element method), the finite-volume method seems to combine the best attributes of the finite-difference method (for simple discrete computational efficiency) and the finite-element method (for geometric flexibility).

To our knowledge, a three-dimensional (3D), unstructured grid, prognostic, primitive equation, finite-volume ocean circulation model is not currently available in the oceanographic community, although some efforts have been made to develop a finite-volume formulation of the two-dimensional, barotropic shallow water equations (Ward 2000). The MIT General Circulation model developed by Marshall et al. (1997a,b) is the first 3D finite-volume ocean model. However, since this model currently relies on rectangular structure grids for horizontal discretization, it is not suited to use for coastal ocean and estuarine domains with complicated geometries. Recently, we have developed a 3D unstructured grid, finite-volume coastal ocean model (called FVCOM). This new model has been applied to the Bohai Sea, a semienclosed coastal ocean, and the Satilla River, a Georgia estuary characterized by numerous tidal creeks and inlets. Compared with results obtained from a well-developed finite-difference model (called ECOM-si) and observational data, we find that the finite-volume model provides a better simulation of tidal elevations and residual currents, especially around islands and tidal creeks. Both FVCOM and ECOM-si show similar distributions of temperature and stratified tidal rectified and buoyancy-induced flows in the interior region in the Bohai Sea, but FVCOM seems to resolve the detailed thermal structure and flows around islands and complex coastal regions.

The remaining sections of this paper are organized as follows. The model formulation, design of unstructured grids, and discretization procedure are described in sections 2, 3, and 4, respectively. The model applications for the Bohai Sea and Satilla River are given and discussed in section 5, and a summary is provided in section 6. Detailed expressions for the numerical computation of individual terms in the momentum equation are given in an appendix.

## 2. The model formulation

### a. The primitive equations

The governing equations consist of the following momentum, continuity, temperature, salinity, and density equations:

$$\begin{aligned} \frac{\partial u}{\partial t} + u \frac{\partial u}{\partial x} + v \frac{\partial u}{\partial y} + w \frac{\partial u}{\partial z} - fv \\ = -\frac{1}{\rho_o} \frac{\partial P}{\partial x} + \frac{\partial}{\partial z} \left( K_m \frac{\partial u}{\partial z} \right) + F_u, \end{aligned} \quad (2.1)$$

$$\begin{aligned} \frac{\partial v}{\partial t} + u \frac{\partial v}{\partial x} + v \frac{\partial v}{\partial y} + w \frac{\partial v}{\partial z} + fu \\ = -\frac{1}{\rho_o} \frac{\partial P}{\partial y} + \frac{\partial}{\partial z} \left( K_m \frac{\partial v}{\partial z} \right) + F_v, \end{aligned} \quad (2.2)$$

$$\frac{\partial P}{\partial z} = -\rho g, \quad (2.3)$$

$$\frac{\partial u}{\partial x} + \frac{\partial v}{\partial y} + \frac{\partial w}{\partial z} = 0, \quad (2.4)$$

$$\begin{aligned} \frac{\partial \theta}{\partial t} + u \frac{\partial \theta}{\partial x} + v \frac{\partial \theta}{\partial y} + w \frac{\partial \theta}{\partial z} \\ = \frac{\partial}{\partial z} \left( K_h \frac{\partial \theta}{\partial z} \right) + F_\theta, \end{aligned} \quad (2.5)$$

$$\begin{aligned} \frac{\partial s}{\partial t} + u \frac{\partial s}{\partial x} + v \frac{\partial s}{\partial y} + w \frac{\partial s}{\partial z} \\ = \frac{\partial}{\partial z} \left( K_h \frac{\partial s}{\partial z} \right) + F_s, \end{aligned} \quad (2.6)$$

$$\rho = \rho(\theta, s), \quad (2.7)$$

where  $x$ ,  $y$ , and  $z$  are the east, north, and vertical axes of the Cartesian coordinate;  $u$ ,  $v$ , and  $w$  are the  $x$ ,  $y$ ,  $z$  velocity components;  $\theta$  is the potential temperature;  $s$  is the salinity;  $\rho$  is the density;  $P$  is the pressure;  $f$  is the Coriolis parameter;  $g$  is the gravitational acceleration;  $K_m$  is the vertical eddy viscosity coefficient; and  $K_h$  is the thermal vertical eddy diffusion coefficient. Here  $F_u$ ,  $F_v$ ,  $F_\theta$ , and  $F_s$  represent the horizontal momentum, thermal, and salt diffusion terms.

Here  $K_m$  and  $K_h$  are parameterized using the Mellor and Yamada (1982) level-2.5 (MY-2.5) turbulent closure scheme as modified by Galperin et al. (1988). In the boundary layer approximation where the shear production of turbulent kinetic energy is produced by the vertical shear of the horizontal flow near the boundary, the equations for  $q^2$  and  $q^2l$  can be simplified as

$$\begin{aligned} \frac{\partial q^2}{\partial t} + u \frac{\partial q^2}{\partial x} + v \frac{\partial q^2}{\partial y} + w \frac{\partial q^2}{\partial z} \\ = 2(P_s + P_b - \epsilon) + \frac{\partial}{\partial z} \left( K_q \frac{\partial q^2}{\partial z} \right) + F_q, \end{aligned} \quad (2.8)$$

$$\begin{aligned} \frac{\partial q^2 l}{\partial t} + u \frac{\partial q^2 l}{\partial x} + v \frac{\partial q^2 l}{\partial y} + w \frac{\partial q^2 l}{\partial z} \\ = lE_1 \left( P_s + P_b - \frac{\tilde{W}}{E_1} \epsilon \right) + \frac{\partial}{\partial z} \left( K_q \frac{\partial q^2 l}{\partial z} \right) + F_l, \end{aligned} \quad (2.9)$$

where  $q^2 = (u'^2 + v'^2)/2$  is the turbulent kinetic energy;  $l$  is the turbulent macroscale;  $K_q$  is the vertical eddy diffusion coefficient of the turbulent kinetic energy;  $F_q$  and  $F_l$  represent the horizontal diffusion of the turbulent kinetic energy and macroscale;  $P_s = K_m(u_z^2 + v_z^2)$  and  $P_b = (gK_h\rho_z)/\rho_o$  are the shear and buoyancy production terms of turbulent kinetic energy;  $\varepsilon = q^3/B_1l$  is the turbulent kinetic energy dissipation rate;  $W = 1 + E_2l^2/(\kappa L)^2$  is a wall proximity function, where  $L^{-1} = (\zeta - z)^{-1} + (H + z)^{-1}$ ;  $\kappa = 0.4$  is the von Kármán constant;  $H$  is the mean water depth; and  $\zeta$  is the free surface elevation. In general,  $F_q$  and  $F_l$  are kept as small as possible to reduce the effects of horizontal diffusion on the solutions.

The turbulent kinetic energy and macroscale equations are closed by defining

$$K_m = lqS_m, \quad K_h = lqS_h, \quad K_q = 0.2lq. \quad (2.10)$$

The stability functions  $S_m$  and  $S_h$  are defined as

$$S_m = \frac{0.4275 - 3.354G_h}{(1 - 34.676G_h)(1 - 6.127G_h)} \quad \text{and}$$

$$S_h = \frac{0.494}{1 - 34.676G_h}, \quad (2.11)$$

where  $G_h = (l^2g/q^2\rho_o)\rho_z$ . In the original MY level-2.5 turbulent closure model (Mellor and Yamada 1974, 1982),  $S_m$  and  $S_h$  are functions of the gradient Richardson number. By removing a slight inconsistency in the scaling analysis, Galperin et al. (1988) simplified the MY turbulent closure model so that  $S_m$  and  $S_h$  depend only on  $G_h$ . Here  $G_h$  has an upper bound of 0.023 for the case of unstable ( $\rho_z > 0$ ) stratification and a lower bound of  $-0.28$  for the case of stable ( $\rho_z < 0$ ) stratification. Parameters  $A_1$ ,  $A_2$ ,  $B_1$ ,  $B_2$ , and  $C_1$  are given as 0.92, 16.6, 0.74, 10.1, and 0.08, respectively.

The surface and bottom boundary conditions for  $u$ ,  $v$ , and  $w$  are

$$K_m \left( \frac{\partial u}{\partial z}, \frac{\partial v}{\partial z} \right) = \frac{1}{\rho_o} (\tau_{sx}, \tau_{sy}),$$

$$w = \frac{\partial \zeta}{\partial t} + u \frac{\partial \zeta}{\partial x} + v \frac{\partial \zeta}{\partial y},$$

at  $z = \zeta(x, y, t)$ , and (2.12)

$$K_m \left( \frac{\partial u}{\partial z}, \frac{\partial v}{\partial z} \right) = \frac{1}{\rho_o} (\tau_{bx}, \tau_{by}),$$

$$w = -u \frac{\partial H}{\partial x} - v \frac{\partial H}{\partial y},$$

at  $z = -H(x, y)$ , (2.13)

where  $(\tau_{sx}, \tau_{sy})$  and  $(\tau_{bx}, \tau_{by}) = C_d \sqrt{u^2 + v^2}(u, v)$  are the  $x$  and  $y$  components of surface wind and bottom stresses;  $D = H + \zeta$ . The drag coefficient  $C_d$  is

determined by matching a logarithmic bottom layer to the model at a height  $z_{ab}$  above the bottom; that is,

$$C_d = \max \left[ \frac{k^2}{\ln \left( \frac{z_{ab}}{z_o} \right)^2}, 0.0025 \right], \quad (2.14)$$

where  $k = 0.4$  is the von Kármán's constant and  $z_o$  is the bottom roughness parameter.

The surface and bottom boundary conditions for temperature are

$$\frac{\partial \theta}{\partial z} = \frac{1}{\rho c_p K_h} [Q_n(x, y, t) - \text{SW}(x, y, \zeta, t)],$$

at  $z = \zeta(x, y, t)$ , (2.15)

$$\frac{\partial \theta}{\partial z} = 0, \quad \text{at } z = -H(x, y), \quad (2.16)$$

where  $Q_n(x, y, t)$  is the surface net heat flux, which consists of four components: downward shortwave and longwave radiation, and sensible and latent fluxes;  $\text{SW}(x, y, 0, t)$  is the shortwave flux incident at sea surface; and  $c_p$  is the specific heat of seawater. The longwave radiation, and sensible and latent heat fluxes are assumed here to occur at the ocean surface, while the downward shortwave flux  $\text{SW}(x, y, z, t)$  is approximated by

$$\text{SW}(x, y, z, t) = \text{SW}(x, y, 0, t) [\text{Re}^{-z/a} + (1 - R)e^{z/b}], \quad (2.17)$$

where  $a$  and  $b$  are attenuation lengths for longer and shorter (blue-green) wavelength components of the shortwave irradiance, and  $R$  is the percent of the total flux associated with the longer wavelength irradiance. This absorption profile, first suggested by Kraus (1972), has been used in numerical studies of upper-ocean diurnal heating by Simpson and Dickey (1981a,b) and others. The absorption of downward irradiance is included in the temperature (heat) equation in the form of

$$\hat{H}(x, y, z, t) = \frac{\partial \text{SW}(x, y, z, t)}{\partial z}$$

$$= \frac{\text{SW}(x, y, 0, t)}{\rho c_p} \left( \frac{R}{a} e^{-z/a} + \frac{1 - R}{b} e^{z/b} \right). \quad (2.18)$$

This approach leads to a more accurate prediction of near-surface temperature than the flux formulation based on a single wavelength approximation (Chen et al. 2002).

The surface and bottom boundary conditions for salinity are

$$\frac{\partial s}{\partial z} = \frac{s(\hat{P} - \hat{E})}{K_n \rho} \quad \text{at } z = \zeta(x, y, t) \quad \text{and} \quad v_n = 0; \quad \frac{\partial \theta}{\partial n} = 0; \quad \frac{\partial s}{\partial n} = 0, \quad (2.22)$$

$$\frac{\partial s}{\partial z} = 0 \quad \text{at } z = -H(x, y), \quad (2.19)$$

where  $\hat{P}$  and  $\hat{E}$  are precipitation and evaporation rates, respectively. Note that a groundwater flux can be easily added into the model by modifying the bottom boundary conditions for vertical velocity and salinity.

The surface and bottom boundary conditions for the turbulent kinetic energy and macroscale equations are

$$q^2 l = 0, \quad q^2 = B_1^{2/3} u_{\tau s}^2 \quad \text{at } z = \zeta(x, y, t), \quad (2.20)$$

$$q^2 l = 0, \quad q^2 = B_1^{2/3} u_{\tau b}^2 \quad \text{at } z = -H(x, y), \quad (2.21)$$

where  $u_{\tau s}$  and  $u_{\tau b}$  are the friction velocities associated with the surface and bottom stresses.

The kinematic and heat and salt conditions on the solid boundary are specified as

where  $v_n$  is the velocity component normal to the boundary, and  $n$  is the coordinate normal to the boundary.

### b. The governing equations in the $\sigma$ coordinate

The  $\sigma$ -coordinate transformation is used in the vertical in order to obtain a smooth representation of irregular bottom topography. The  $\sigma$ -coordinate transformation is defined as

$$\sigma = \frac{z - \zeta}{H + \zeta} = \frac{z - \zeta}{D}, \quad (2.23)$$

where  $\sigma$  varies from  $-1$  at the bottom to  $0$  at the surface. In this coordinate, equations (2.1)–(2.9) are given as

$$\begin{aligned} \frac{\partial u D}{\partial t} + \frac{\partial u^2 D}{\partial x} + \frac{\partial uv D}{\partial y} + \frac{\partial u \omega}{\partial \sigma} - f v D = -g D \frac{\partial \zeta}{\partial x} - \frac{g D}{\rho_o} \left[ \frac{\partial}{\partial x} \left( D \int_{\sigma}^0 \rho \, d\sigma' \right) + \sigma \rho \frac{\partial D}{\partial x} \right] \\ + \frac{1}{D} \frac{\partial}{\partial \sigma} \left( K_m \frac{\partial u}{\partial \sigma} \right) + DF_x, \end{aligned} \quad (2.24)$$

$$\begin{aligned} \frac{\partial v D}{\partial t} + \frac{\partial uv D}{\partial x} + \frac{\partial v^2 D}{\partial y} + \frac{\partial v \omega}{\partial \sigma} + f u D = -g D \frac{\partial \zeta}{\partial y} - \frac{g D}{\rho_o} \left[ \frac{\partial}{\partial y} \left( D \int_{\sigma}^0 \rho \, d\sigma' \right) + \sigma \rho \frac{\partial D}{\partial y} \right] \\ + \frac{1}{D} \frac{\partial}{\partial \sigma} \left( K_m \frac{\partial v}{\partial \sigma} \right) + DF_y, \end{aligned} \quad (2.25)$$

$$\frac{\partial \theta D}{\partial t} + \frac{\partial \theta u D}{\partial x} + \frac{\partial \theta v D}{\partial y} + \frac{\partial \theta \omega}{\partial \sigma} = \frac{1}{D} \frac{\partial}{\partial \sigma} \left( K_h \frac{\partial \theta}{\partial \sigma} \right) + D \hat{H} + DF_{\theta}, \quad (2.26)$$

$$\frac{\partial s D}{\partial t} + \frac{\partial s u D}{\partial x} + \frac{\partial s v D}{\partial y} + \frac{\partial s \omega}{\partial \sigma} = \frac{1}{D} \frac{\partial}{\partial \sigma} \left( K_h \frac{\partial s}{\partial \sigma} \right) + DF_s, \quad (2.27)$$

$$\frac{\partial q^2 D}{\partial t} + \frac{\partial q^2 u D}{\partial x} + \frac{\partial q^2 v D}{\partial y} + \frac{\partial q^2 \omega}{\partial \sigma} = 2D(P_s + P_b - \varepsilon) + \frac{1}{D} \frac{\partial}{\partial \sigma} \left( K_q \frac{\partial q^2}{\partial \sigma} \right) + DF_q, \quad (2.28)$$

$$\frac{\partial q^2 l D}{\partial t} + \frac{\partial q^2 l u D}{\partial x} + \frac{\partial q^2 l v D}{\partial y} + \frac{\omega}{D} \frac{\partial q^2 l \omega}{\partial \sigma} = l E_1 D \left( P_s + P_b - \frac{\tilde{W}}{E_1} \varepsilon \right) + \frac{1}{D} \frac{\partial}{\partial \sigma} \left( K_q \frac{\partial q^2 l}{\partial \sigma} \right) + DF_l, \quad (2.29)$$

$$\rho = \rho(\theta, s). \quad (2.30)$$

The horizontal diffusion terms are defined as

$$DF_x \approx \frac{\partial}{\partial x} \left[ 2A_m H \frac{\partial u}{\partial x} \right] + \frac{\partial}{\partial y} \left[ A_m H \left( \frac{\partial u}{\partial y} + \frac{\partial v}{\partial x} \right) \right], \quad (2.32)$$

$$DF_y \approx \frac{\partial}{\partial x} \left[ A_m H \left( \frac{\partial u}{\partial y} + \frac{\partial v}{\partial x} \right) \right] + \frac{\partial}{\partial y} \left[ 2A_m H \frac{\partial v}{\partial y} \right], \quad (2.33)$$

$$D(F_{\theta}, F_s, F_{q^2}, F_{q^2 l})$$

$$\approx \left[ \frac{\partial}{\partial x} \left( A_h H \frac{\partial}{\partial x} \right) + \frac{\partial}{\partial y} \left( A_h H \frac{\partial}{\partial y} \right) \right] (\theta, s, q^2, q^2 l), \quad (2.34)$$

where  $A_m$  and  $A_h$  are the horizontal eddy and thermal diffusion coefficients, respectively. Following the finite-

difference primitive equation coastal ocean models (called POM and ECOM-si) developed originally by Blumberg and Mellor (1987), this definition ensures the validity of the bottom boundary layer simulation in the  $\sigma$ -coordinate transformation system. The detailed description was given in Mellor and Blumberg (1985).

The boundary conditions are given as follows. At the surface where  $\sigma = 0$ ,

$$\begin{aligned} \left( \frac{\partial u}{\partial \sigma}, \frac{\partial v}{\partial \sigma} \right) &= \frac{D}{\rho_o K_m} (\tau_{sx}, \tau_{sy}), \quad \omega = 0, \\ \frac{\partial \theta}{\partial \sigma} &= \frac{D}{\rho_c K_h} [Q_n(x, y, t) - SW(x, y, 0, t)], \\ \frac{\partial s}{\partial \sigma} &= -\frac{s(P - E)D}{K_h}, \quad q^2 l = 0, \\ q^2 &= B_1^{2/3} u_{\tau s}^2, \end{aligned} \quad (2.35)$$

and at the bottom where  $\sigma = -1$

$$\begin{aligned} \left( \frac{\partial u}{\partial \sigma}, \frac{\partial v}{\partial \sigma} \right) &= \frac{D}{\rho_o K_m} (\tau_{bx}, \tau_{by}), \quad \omega = 0, \\ \frac{\partial \theta}{\partial \sigma} &= \frac{\partial s}{\partial \sigma} = 0, \quad q^2 l = 0, \\ q^2 &= B_1^{2/3} u_{\tau b}^2. \end{aligned} \quad (2.36)$$

*c. The 2D (vertically integrated) equations*

The sea surface elevation included in the equations describes the fast-moving surface gravity waves. In the explicit numerical approach, the criterion for the time step is inversely proportional to the phase speed of these waves. Since the sea surface elevation is proportional to the gradient of water transport, it can be computed using vertically integrated equations. The 3D equations then can be solved under conditions with a given sea surface elevation. In this numerical method, called ‘‘mode splitting,’’ the currents are divided into external and internal modes that can be computed using two distinct time steps. This approach is used successfully in POM.

Recently, a semi-implicit scheme was introduced into POM, in which the sea surface elevation was computed implicitly using a preconditioned conjugate gradient method with no sacrifice in computational time (Casulli and Cheng 1991). This updated version of POM is called ECOM-si. The semi-implicit scheme cannot easily be applied to a finite-volume model since it is difficult to construct a linear positive symmetric algebraic matrix when unstructured triangular meshes are used. For this reason, we select the mode-splitting method to solve the momentum equations.

The 2D (vertically integrated) momentum and continuity equations are given as

$$\frac{\partial \zeta}{\partial t} + \frac{\partial(\bar{u}D)}{\partial x} + \frac{\partial(\bar{v}D)}{\partial y} = 0, \quad (2.37)$$

$$\begin{aligned} \frac{\partial \bar{u}D}{\partial t} + \frac{\partial \bar{u}^2 D}{\partial x} + \frac{\partial \bar{u}\bar{v}D}{\partial y} - f\bar{v}D &= -gD \frac{\partial \zeta}{\partial x} - \frac{gD}{\rho_o} \left\{ \int_{-1}^0 \frac{\partial}{\partial x} \left( D \int_{\sigma}^0 \rho d\sigma' \right) d\sigma + \frac{\partial D}{\partial x} \int_{-1}^0 \sigma \rho d\sigma \right\} \\ &+ \frac{\partial_{xx} - \tau_{bx}}{\rho_o} + D\tilde{F}_x + G_x, \end{aligned} \quad (2.38)$$

$$\begin{aligned} \frac{\partial \bar{v}D}{\partial t} + \frac{\partial \bar{u}\bar{v}D}{\partial x} + \frac{\partial \bar{v}^2 D}{\partial y} + f\bar{u}D &= -gD \frac{\partial \zeta}{\partial y} - \frac{gD}{\rho_o} \left\{ \int_{-1}^0 \frac{\partial}{\partial y} \left( D \int_{\sigma}^0 \rho d\sigma' \right) d\sigma + \frac{\partial D}{\partial y} \int_{-1}^0 \sigma \rho d\sigma \right\} \\ &+ \frac{\tau_{sy} - \tau_{by}}{\rho_o} + D\tilde{F}_y + G_y, \end{aligned} \quad (2.39)$$

where  $G_x$  and  $G_y$  are defined as

$$\begin{aligned} G_x &= \frac{\partial \bar{u}^2 D}{\partial x} + \frac{\partial \bar{u}\bar{v}D}{\partial y} - D\tilde{F}_x \\ &- \left[ \frac{\partial \bar{u}^2 D}{\partial x} + \frac{\partial \bar{u}\bar{v}D}{\partial y} - D\bar{F}_x \right], \end{aligned} \quad (2.40)$$

$$\begin{aligned} G_y &= \frac{\partial \bar{u}\bar{v}D}{\partial x} + \frac{\partial \bar{v}^2 D}{\partial y} - D\tilde{F}_y \\ &- \left[ \frac{\partial \bar{u}\bar{v}D}{\partial x} + \frac{\partial \bar{v}^2 D}{\partial y} - D\bar{F}_y \right], \end{aligned} \quad (2.41)$$

and the horizontal diffusion terms are approximately given as

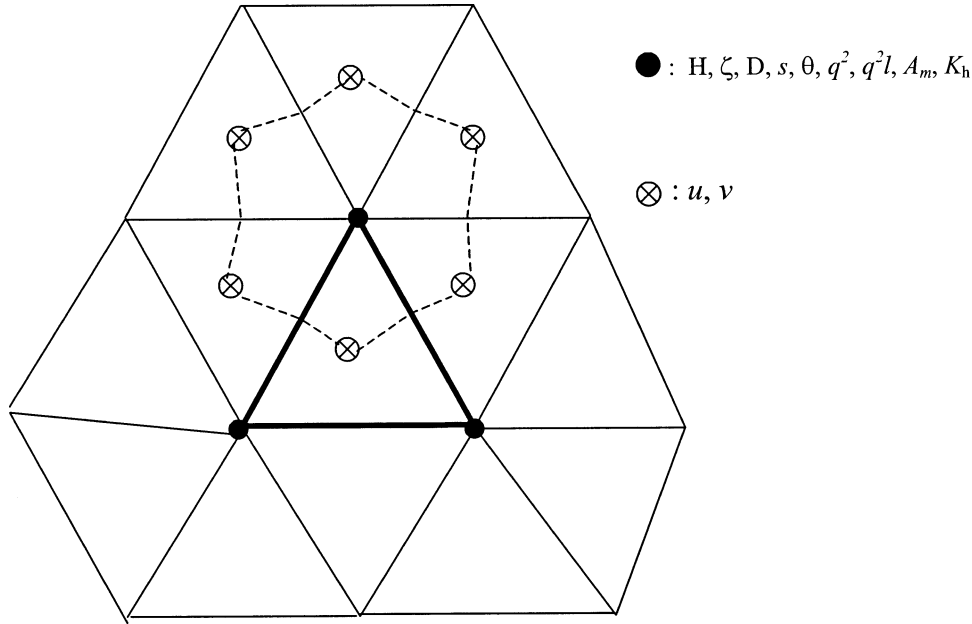


FIG. 1. The unstructured grid for the finite-volume model.

$$D\tilde{F}_x \approx \frac{\partial}{\partial x} \left[ 2\bar{A}_m H \frac{\partial \bar{u}}{\partial x} \right] + \frac{\partial}{\partial y} \left[ \bar{A}_m H \left( \frac{\partial \bar{u}}{\partial y} + \frac{\partial \bar{v}}{\partial x} \right) \right], \quad (2.42)$$

$$D\tilde{F}_y \approx \frac{\partial}{\partial x} \left[ \bar{A}_m H \left( \frac{\partial \bar{u}}{\partial y} + \frac{\partial \bar{v}}{\partial x} \right) \right] + \frac{\partial}{\partial y} \left[ 2\bar{A}_m H \frac{\partial \bar{v}}{\partial y} \right], \quad (2.43)$$

$$D\bar{F}_x \approx \frac{\partial}{\partial x} \overline{2A_m H \frac{\partial u}{\partial x}} + \frac{\partial}{\partial y} \overline{A_m H \left( \frac{\partial u}{\partial y} + \frac{\partial v}{\partial x} \right)}, \quad (2.44)$$

$$D\bar{F}_y \approx \frac{\partial}{\partial x} \overline{A_m H \left( \frac{\partial u}{\partial y} + \frac{\partial v}{\partial x} \right)} + \frac{\partial}{\partial y} \overline{2A_m H \frac{\partial v}{\partial y}}. \quad (2.45)$$

The overbar “ $\bar{\quad}$ ” denotes the vertically integration. For example, for a given variable  $\psi$ ,

$$\bar{\psi} = \int_{-1}^0 \psi d\sigma. \quad (2.46)$$

### 3. Design of the unstructured grids

Similar to the finite-element method, the horizontal numerical computational domain is subdivided into a set of nonoverlapping unstructured triangular cells. An unstructured triangle comprises three nodes, a centroid, and three sides (Fig. 1). Let  $N$  and  $M$  be the total number of centroids and nodes in the computational domain, respectively, then the locations of centroids can be expressed as

$$[X(i), Y(i)], \quad i = 1:N; \quad (3.1)$$

and the locations of nodes can be specified as

$$[X_n(j), Y_n(j)], \quad j = 1:M. \quad (3.2)$$

Since none of the triangles in the grid overlap,  $N$  should also be the total number of unstructured triangles. On each triangle cell, the three nodes are identified using integral numbers defined as  $N_i(\hat{j})$ , where  $\hat{j}$  is counted clockwise from 1 to 3. The surrounding triangles that have a common side are counted using integral numbers defined as  $NBE_i(\hat{j})$ , where  $\hat{j}$  is counted clockwise from 1 to 3. At open or coastal solid boundaries,  $NBE_i(\hat{j})$  is specified as zero. At each node, the total number of the surrounding triangles with a connection to this node is expressed as  $NT(j)$ , and they are counted using integral numbers  $NB_i(m)$ , where  $m$  is counted clockwise from 1 to  $NT(j)$ .

To provide a more accurate estimation of the sea surface elevation, currents, and salt and temperature fluxes, the numerical computation is conducted in a specially designed triangular grid in which  $\zeta$ ,  $\omega$ ,  $s$ ,  $\theta$ ,  $\rho$ ,  $q^2$ ,  $q^2l$ ,  $H$ ,  $D$ ,  $K_m$ ,  $K_h$ ,  $A_m$ , and  $A_h$  are placed at nodes, and  $u$ ,  $v$  are placed at centroids. Variables at each node are determined by a net flux through the sections linked to centroids in the surrounding triangles with connection to that node. Variables at centroids are calculated based on a net flux through three sides of that triangle. The numerical code was written using Fortran 77 and can be run on a PC or workstation with Fortran 77 or above.

### 4. The discretization procedure

#### a. The 2D external mode

Let us consider the continuity equation first. Integrating Eq. (2.37) over a given triangle area yields

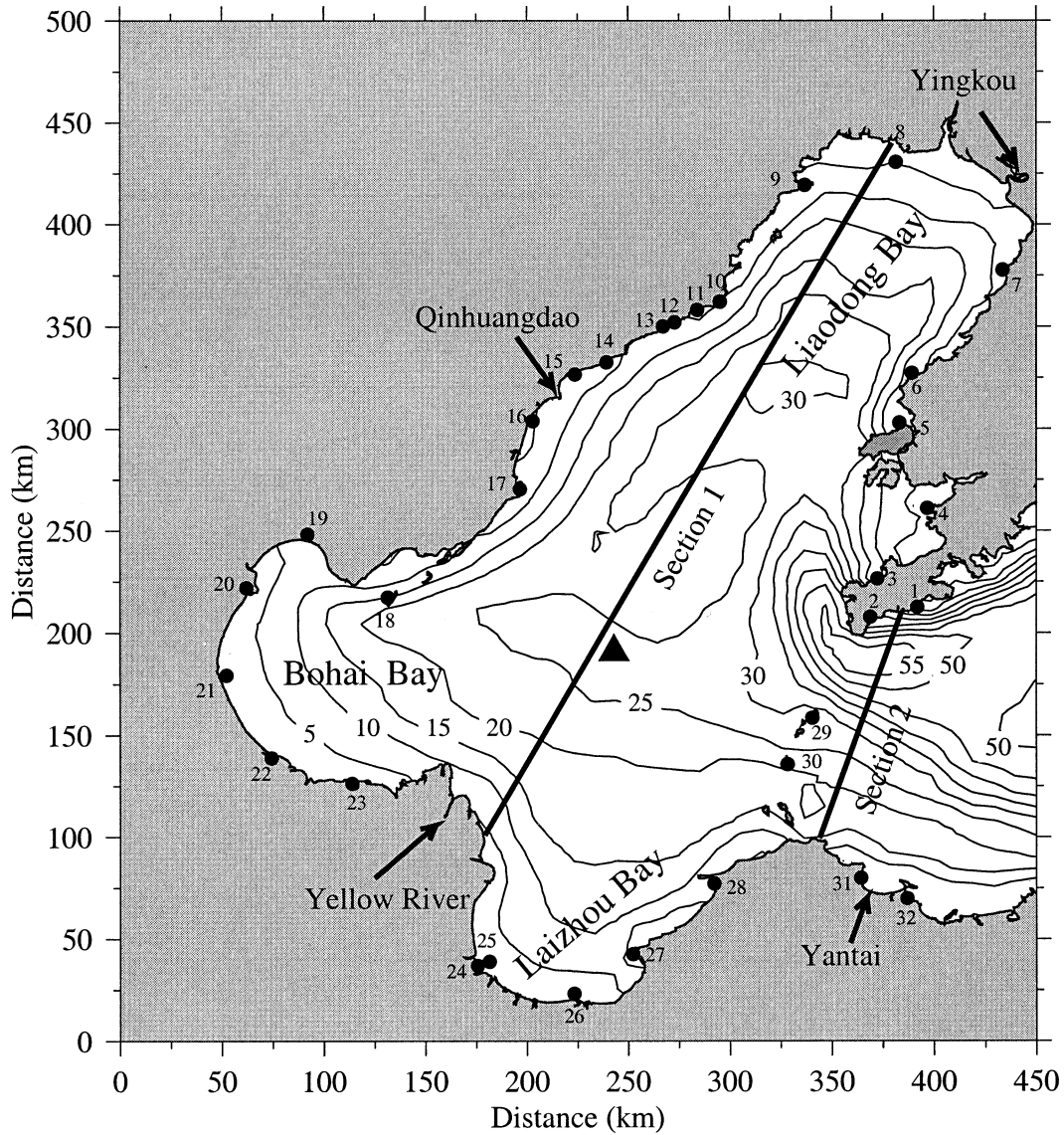


FIG. 2. Geometry of the Bohai Sea. Filled dots with numbers 1–32 shown along the coast are tidal measurement stations. Two heavy solid lines and filled triangles are the sections and site used for model comparisons.

$$\iint \frac{\partial \zeta}{\partial t} dx dy = - \iint \left[ \frac{\partial(\bar{u}D)}{\partial x} + \frac{\partial(\bar{v}D)}{\partial y} \right] dx dy$$

$$= - \oint_{s'} \bar{v}_n D ds', \quad (4.1)$$

where  $\bar{v}_n$  is the velocity component normal to the sides of the triangle and  $s'$  is the closed trajectory that comprises the three sides. Equation (4.1) is integrated numerically using the modified fourth-order Runge–Kutta time-stepping scheme. This is a modified multistage time-stepping approach with second-order accuracy (Dick 1994). The detailed procedure for this method is described as follows:

$$\zeta_j^0 = \zeta_j^n,$$

$$R_\zeta^0 = R_\zeta^n = \sum_{m=1}^{NT(j)} [(\Delta x_{2m-1} \bar{v}_m^n - \Delta y_{2m-1} \bar{u}_m^n) D_{2m-1}^n + (\Delta x_{2m} \bar{v}_m^n - \Delta y_{2m} \bar{u}_m^n) D_{2m}^n], \quad (4.2)$$

$$\zeta_j^k = \zeta_j^0 - \alpha^k \frac{\Delta t R_\zeta^{k-1}}{2\Omega_j^k}, \quad \text{and} \quad \zeta_j^{n+1} = \zeta_j^4, \quad (4.3)$$

where  $k = 1, 2, 3, 4$  and  $(\alpha^1, \alpha^2, \alpha^3, \alpha^4) = (1/4, 1/3, 1/2, 1)$ . Superscript  $n$  represents the  $n$ th time step. Here  $\Omega_j^k$  is the area enclosed by the lines through centroids and midpoints of side of surrounding triangles connected to the node where  $\zeta_j$  is located. Also  $\bar{u}_m^n$  and  $\bar{v}_m^n$  are defined as

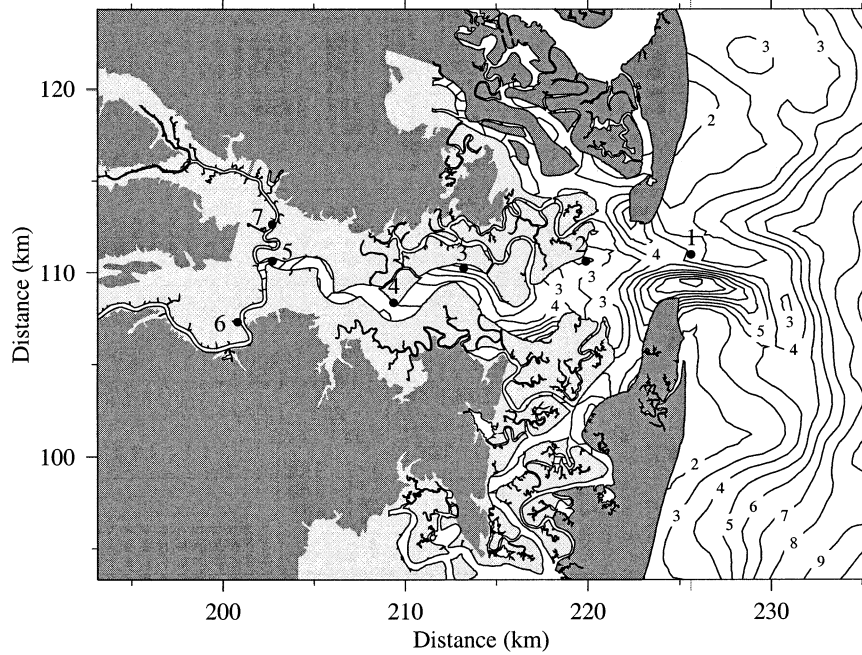


FIG. 3. Geometry of the Satilla River. Water depth contours are in meters. Filled dots are seven bottom pressure measurement sites conducted by Dr. Blanton at Skidaway Institute of Oceanography, Savannah, GA.

$$\bar{u}_m^n = \overline{u[NT(m)]^n}, \quad \bar{v}_m^n = \overline{v[NT(m)]^n}. \quad (4.4) \quad \Delta y_{2m-1} = y_{2m} - y_{2m-1}, \quad \Delta y_{2m} = y_{2m+1} - y_{2m}. \quad (4.6)$$

The time step for the external mode is  $\Delta t$  and

$$\Delta x_{2m-1} = x_{2m} - x_{2m-1}, \quad \Delta x_{2m} = x_{2m+1} - x_{2m}, \quad (4.5)$$

Similarly, integrating Eqs. (2.38) and (2.39) over a given triangle area, we get

$$\begin{aligned} \iint \frac{\partial \bar{u} D}{\partial t} dx dy &= -\oint_{s'} \bar{u} D \bar{v}_n ds' + \iint f \bar{v} D dx dy - \iint g D \frac{\partial \zeta}{\partial x} dx dy \\ &\quad - \iint \left\{ \frac{g D^2}{\rho_o} \int_{-1}^0 \left[ \frac{\partial}{\partial x} \int_{\sigma}^0 \rho d\sigma - \int_{\sigma}^0 \frac{\partial \rho}{\partial \sigma} \frac{\sigma}{D} \frac{\partial D}{\partial x} d\sigma \right] d\sigma \right\} dx dy \\ &\quad + \iint \frac{\tau_{sx} - \tau_{bx}}{\rho_o} dx dy + \iint D \bar{F}_x dx dy + \iint G_x dx dy, \end{aligned} \quad (4.7)$$

$$\begin{aligned} \iint \frac{\partial \bar{v} D}{\partial t} dx dy &= -\oint_{s'} \bar{v} D \bar{v}_n ds' - \iint f \bar{u} D dx dy - \iint g D \frac{\partial \zeta}{\partial y} dx dy \\ &\quad - \iint \left\{ \frac{g D^2}{\rho_o} \int_{-1}^0 \left[ \frac{\partial}{\partial y} \int_{\sigma}^0 \rho d\sigma - \int_{\sigma}^0 \frac{\partial \rho}{\partial \sigma} \frac{\sigma}{D} \frac{\partial D}{\partial y} d\sigma \right] d\sigma \right\} dx dy \\ &\quad + \iint \frac{\tau_{sy} - \tau_{by}}{\rho_o} dx dy + \iint D \bar{F}_y dx dy + \iint G_y dx dy. \end{aligned} \quad (4.8)$$

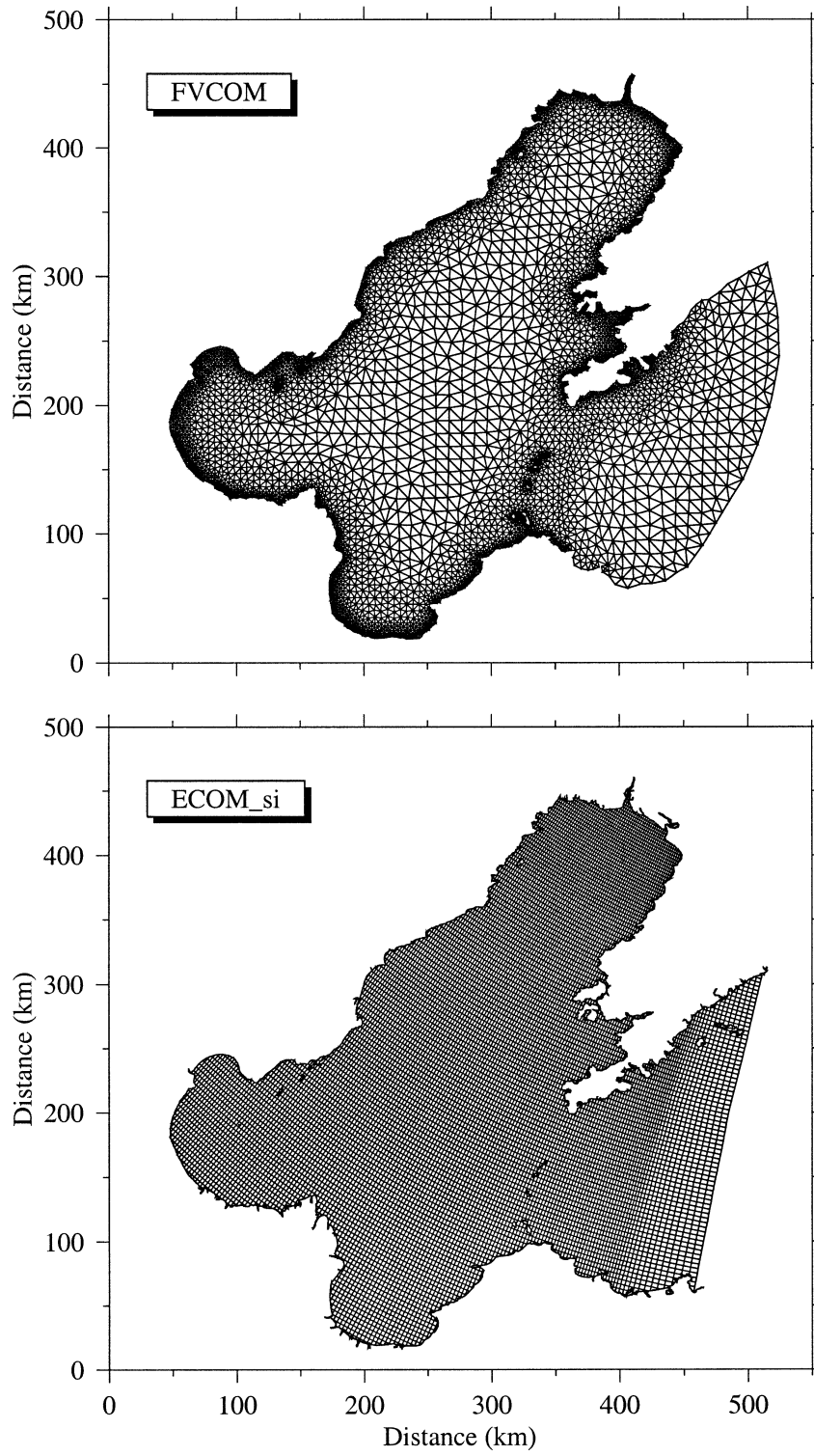


FIG. 4. Unstructured and curvilinear grids of the Bohai Sea for FVCOM and ECOM-si.

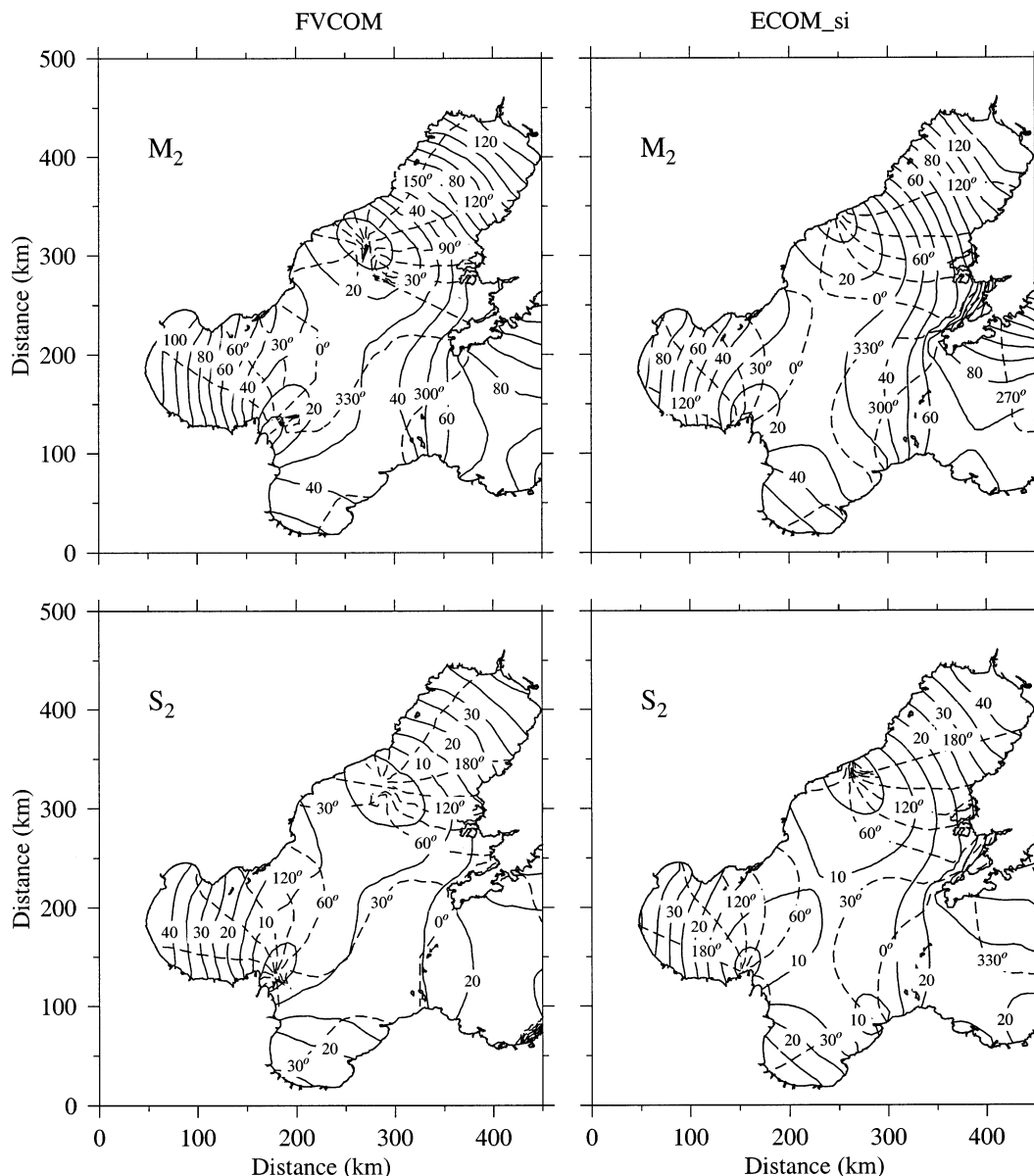


FIG. 5. The charts of model-predicted coamplitudes and cophases of the  $M_2$  and  $S_2$  tides in the Bohai Sea. (right) ECOM-si and (left) FVCOM.

Equations (4.7) and (4.8) are also integrated numerically using the modified fourth-order Runge–Kutta time-stepping scheme as follows:

$$\begin{aligned} \bar{u}_i^0 &= \bar{u}_i^n, & \bar{v}_i^0 &= \bar{v}_i^n, & \bar{R}_u^0 &= \bar{R}_u^n, \\ \bar{R}_v^0 &= \bar{R}_v^n, \end{aligned} \tag{4.9}$$

$$\begin{aligned} \bar{u}_i^k &= \bar{u}_i^0 - \alpha^k \frac{\Delta t \bar{R}_u^0}{4\Omega_i^u \bar{D}_i}, \\ \bar{v}_i^k &= \bar{v}_i^0 - \alpha^k \frac{\Delta t \bar{R}_v^0}{4\Omega_i^v \bar{D}_i}, \end{aligned} \tag{4.10}$$

$$\bar{u}_i^{n+1} = \bar{u}_i^4, \quad \bar{v}_i^{n+1} = \bar{v}_i^4, \tag{4.11}$$

where the definitions of  $k$  and  $\alpha^k$  are the same as those shown in Eq. (4.3). Here  $\Omega_i^u$  and  $\Omega_i^v$  are the triangle areas where  $\bar{u}$  and  $\bar{v}$  are located. In the grids used in this model,  $\bar{u}$  and  $\bar{v}$  are all at the centroid, so that  $\Omega_i^u = \Omega_i^v = \Omega_i$ . The depth  $\bar{D}_i$  is at the centroid, which is interpolated from depth values at three nodes. Here  $\bar{R}_u^n$  and  $\bar{R}_v^n$  represent all the terms on the right of Eqs. (4.7) and (4.8), respectively. They are equal to

$$\begin{aligned} \bar{R}_u^n &= ADVU + DPBPX + DPBCX + CORX \\ &+ VISCX - G_x, \end{aligned} \tag{4.12}$$

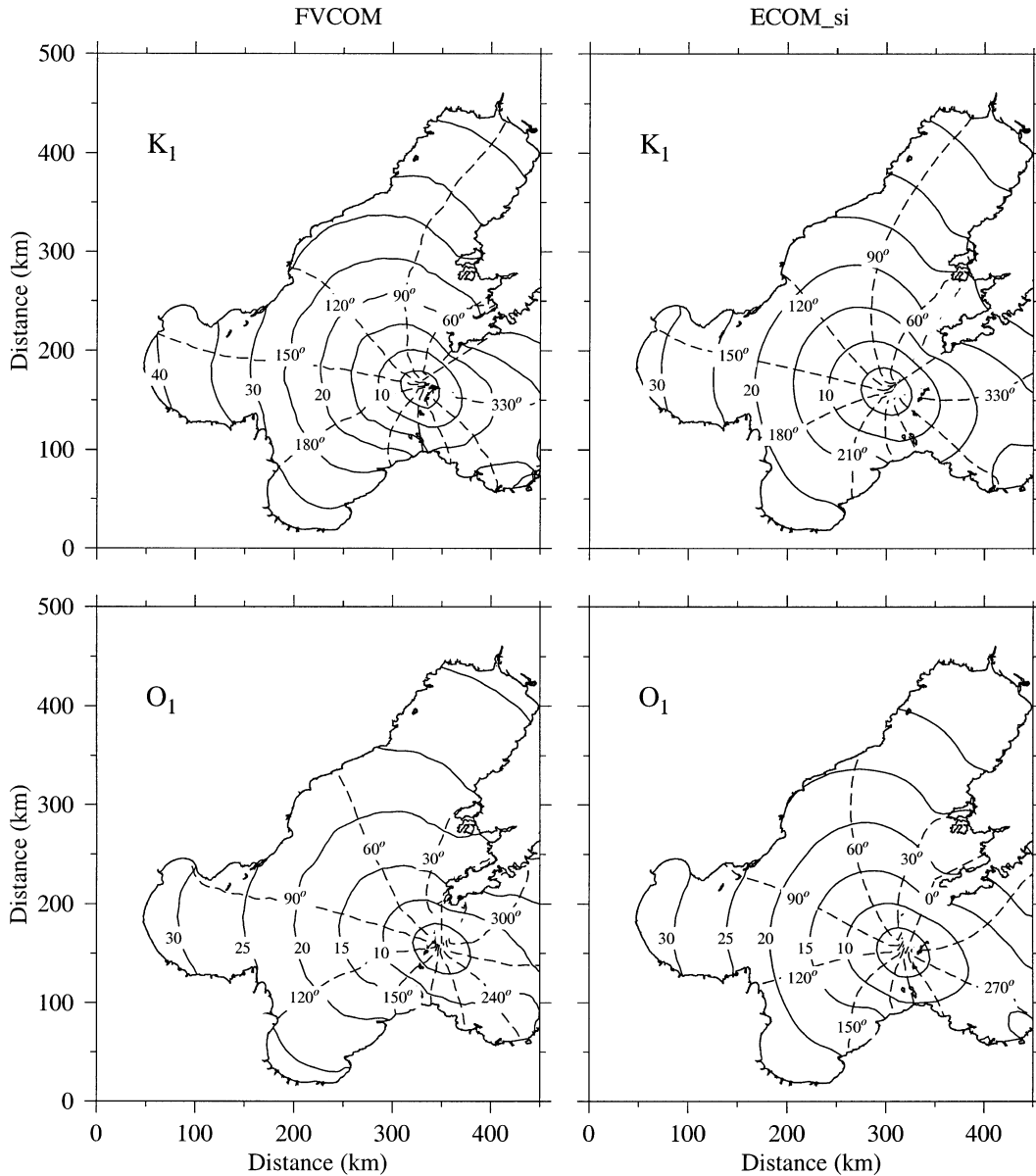


FIG. 6. The charts of model-predicted coamplitudes and cophases of the  $K_1$  and  $O_1$  tides in the Bohai Sea. (right) ECOM-si and (left) FVCOM.

$$\begin{aligned} \bar{R}_v^n = & ADVV + DPBPY + DPBCY + CORY \\ & + VISCY - G_y, \end{aligned} \quad (4.13)$$

where  $ADVU$  and  $ADV V$ ,  $DPBPX$  and  $DPBPY$ ,  $DPBCX$  and  $DPBCY$ ,  $CORX$  and  $CORY$ ,  $VISCX$  and  $VISCY$  are the  $x$  and  $y$  components of vertically integrated horizontal advection, barotropic pressure gradient force, Coriolis force, and horizontal diffusion terms, respectively. The definitions of  $G_x$  and  $G_y$  are the same as those shown in Eqs. (2.40) and (2.41). The numerical approach for these terms is given in the appendix.

*b. The 3D internal mode*

The momentum equations are solved numerically using a simple combined explicit and implicit scheme in which the local change of the currents is integrated using the first-order accuracy upwind scheme. The advection terms are computed explicitly by a second-order accuracy Runge–Kutta time-stepping scheme is also incorporated in the updated version to increase the numerical integration to second-order accuracy. The procedure for this method is very similar to that described above for the 2D external mode. To provide a simple interpretation of the numerical approach for the 3D in-

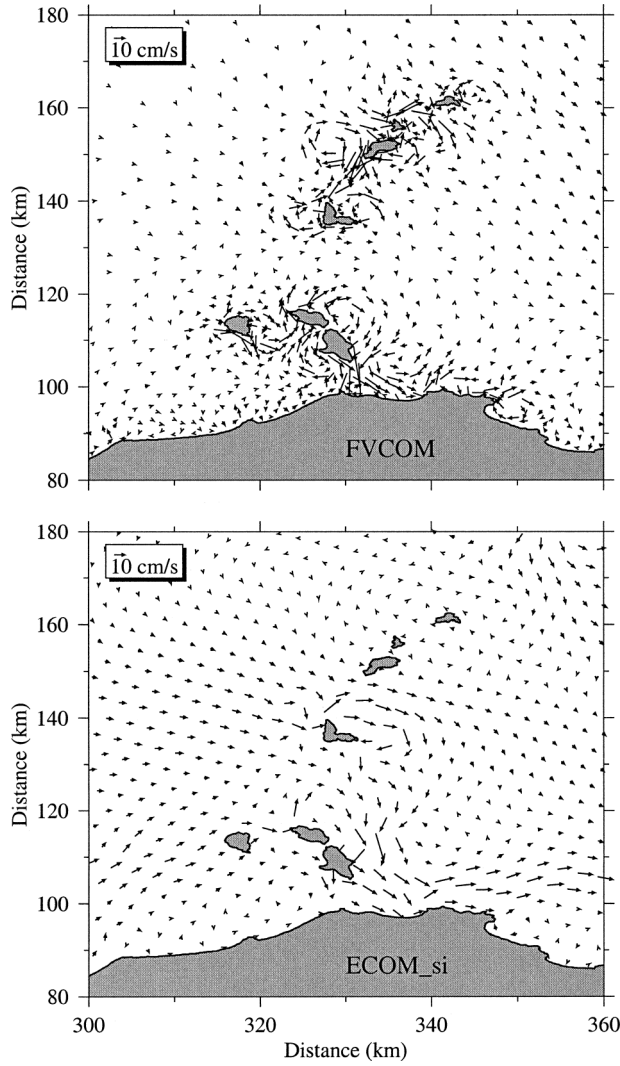


FIG. 7. Distributions of (a) FVCOM and (b) ECOM-si predicted surface residual current vectors around the islands close to the Bohai Sea Strait.

ternal mode, we focus our description here only on the first-order accuracy upwind scheme. It should be noted here that the second-order accuracy Runge–Kutta time-stepping scheme is also incorporated in the model.

The 3D momentum equations can be rewritten as

$$\begin{aligned} \frac{\partial u D}{\partial t} + R_u &= \frac{1}{D} \frac{\partial}{\partial \sigma} \left( K_m \frac{\partial u}{\partial \sigma} \right), \\ \frac{\partial v D}{\partial t} + R_v &= \frac{1}{D} \frac{\partial}{\partial \sigma} \left( K_m \frac{\partial v}{\partial \sigma} \right), \end{aligned} \quad (4.14)$$

where

$$\begin{aligned} R_u &= ADVU3 + CORX3 + DPBPX3 \\ &+ BPBCX3 + HVISCX, \end{aligned} \quad (4.15)$$

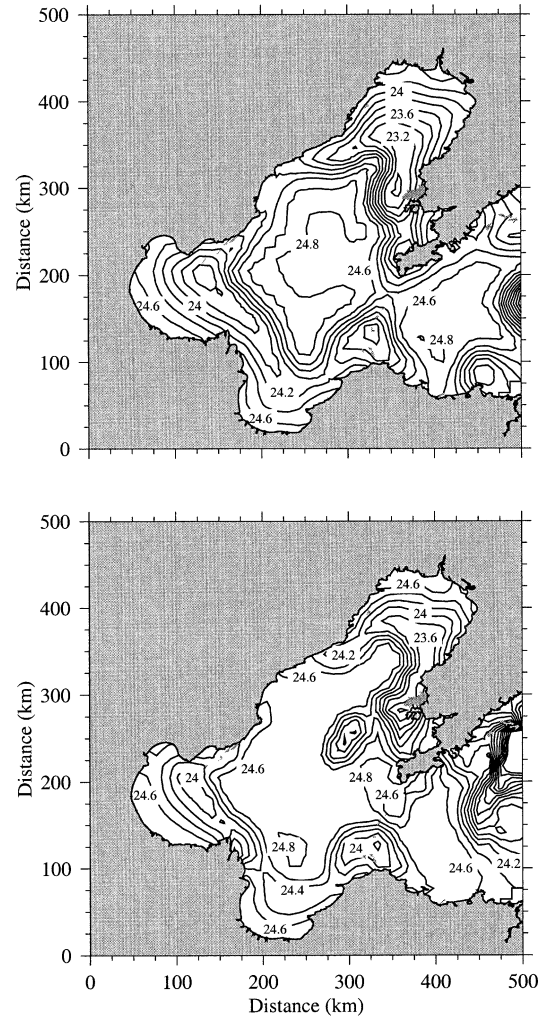


FIG. 8. Distributions of model-predicted near-surface ( $1/2 \sigma$ -level below the surface) temperature averaged over a  $M_2$  tidal cycle of the 10th model day. (top) FVCOM and (bottom) ECOM-si.

$$\begin{aligned} R_v &= ADVV3 + CORY3 + DPBPY3 \\ &+ BPBCY3 + HVISCY. \end{aligned} \quad (4.16)$$

The numerical integration is conducted in two steps. In the first step, the “transition” velocity is calculated using all the terms except the vertical diffusion term in the momentum equations. Then the true velocity is determined implicitly using a balance between the local change of the “transition” velocity and the vertical diffusion term.

Let  $u_{i,k}^*$  and  $v_{i,k}^*$  be the  $x$  and  $y$  components of the “transition” velocity at the midpoint between the  $k$  and  $k + 1$   $\sigma$ -levels in triangular cell  $i$ . They can be determined numerically as follows:

$$\begin{aligned} u_{i,k}^* &= u_{i,k}^n - \frac{\Delta t_l}{\Omega_i \Delta \sigma D_i} R_{u,(i,k)}^n, \\ v_{i,k}^* &= v_{i,k}^n - \frac{\Delta t_l}{\Omega_i \Delta \sigma D_i} R_{v,(i,k)}^n, \end{aligned} \quad (4.17)$$

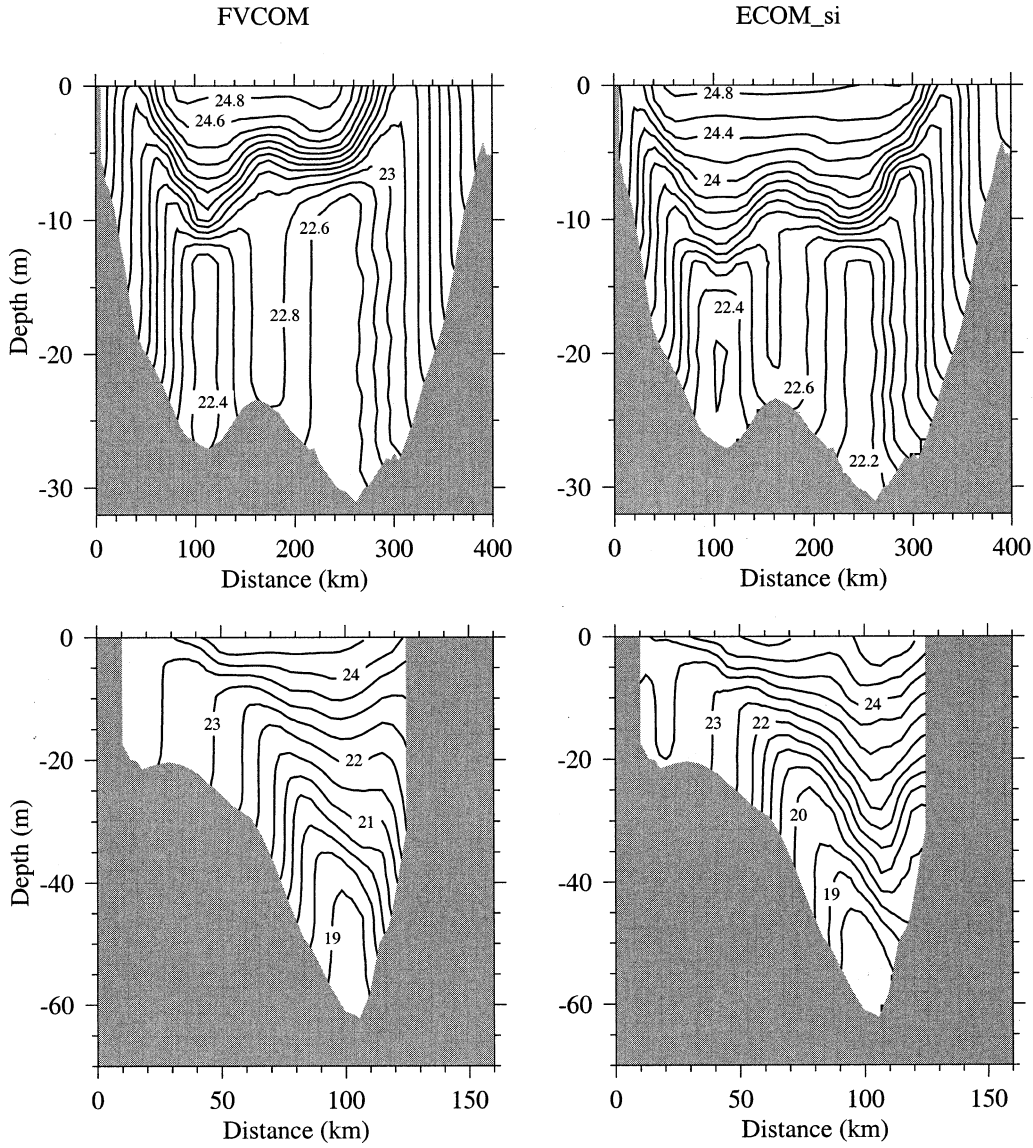


FIG. 9. Vertical distributions of temperature averaged over a  $M_2$  tidal cycle of the 10th model day on cross-sea sections 1 and 2. (right) ECOM-si and (left) FVCOM.

where  $\Delta\sigma = \sigma_k - \sigma_{k+1}$ , and  $\Delta t_i$  is the time step for the internal mode. The numerical approach for computing  $R_{u,(i,k)}^n$  and  $R_{v,(i,k)}^n$  is described in detail in the appendix.

After the transition velocity is determined, the true velocity ( $u_{i,k}^{n+1}$  and  $v_{i,k}^{n+1}$ ) at the  $(n + 1)$ th time step can be found by solving the following discrete equation:

$$A_{i,k} u_{i,k+1}^{n+1} + B_{i,k} u_{i,k}^{n+1} + C_{i,k} u_{i,k-1}^{n+1} = u_{i,k}^*, \quad (4.18)$$

$$A_{i,k} v_{i,k+1}^{n+1} + B_{i,k} v_{i,k}^{n+1} + C_{i,k} v_{i,k-1}^{n+1} = v_{i,k}^*, \quad (4.19)$$

where

$$A_{i,k} = -\frac{2K_m(k+1)\Delta t}{[D^{n+1}]^2(\sigma_k - \sigma_{k+1})(\sigma_k - \sigma_{k+2})},$$

$$C_{i,k} = -\frac{2K_m(k)\Delta t}{[D^{n+1}]^2(\sigma_k - \sigma_{k+1})(\sigma_{k-1} - \sigma_{k+1})},$$

$$B_{i,k} = 1 - A_{i,k} - C_{i,k}. \quad (4.20)$$

Equations (4.18) and (4.19) are tridiagonal equations, which can be solved easily for given surface and bottom boundary conditions.

A similar numerical approach is also used to solve the equations for  $\theta$ ,  $s$ ,  $q^2$ , and  $q^2 l$ . For example, the temperature equation can be rewritten as

$$\frac{\partial \theta D}{\partial t} + R_\theta = \frac{1}{D} \frac{\partial}{\partial \sigma} \left( K_h \frac{\partial \theta}{\partial \sigma} \right), \quad (4.21)$$

where

$$R_\theta = \frac{\partial \theta u D}{\partial x} + \frac{\partial \theta v D}{\partial y} + \frac{\partial \theta \omega D}{\partial \sigma} - D\hat{H} - DF_\theta. \quad (4.22)$$

Equation (4.21) is identical to the equations for  $u$  and  $v$  in Eq. (4.14) if  $u$  or  $v$  is replaced by  $\theta$ ,  $R_u$  or  $R_v$  by  $R_\theta$ , and  $K_m$  by  $K_\theta$ . The only difference is that  $\theta$  is calculated at nodes and has the same control volume as that used for  $\zeta$ . To apply a second-order upwind scheme for the temperature advection term, we used Green's theorem to calculate the temperature gradient at nodes (Barth 1993; Wu and Boggy 2000). Computing  $\theta$  at nodes has shown a significant improvement in the advective temperature flux over steep bottom topography. A detailed discussion about this issue will be given in a separate manuscript. The detailed description of the numerical approach for Eq. (4.21) is given in the appendix.

## 5. Model applications

To test our new unstructured grid, finite-volume, ocean circulation model, we applied it to the Bohai Sea around the northern coast of China and the Satilla River in the inner shelf of the South Atlantic Bight. The Bohai Sea is a semienclosed coastal ocean that includes multiple islands and coastal inlets (Fig. 2). The mean depth of the Bohai is about 20 m, with the deepest region of about 70 m located near the northern coast of the Bohai Strait. The Satilla River is a typical estuary characterized by complex curved coastlines, multiple tidal creeks and inlets (Fig. 3). The mean depth of this river is about 4 m, with the deepest region being about 20 m near the river mouth.

In the Bohai Sea, the motion is dominated by semi-diurnal ( $M_2$  and  $S_2$ ) and diurnal ( $K_1$  and  $O_1$ ) tides, which account for about 60% of the current variation and kinetic energy there. Since the tidally rectified residual flow is only substantial near the coast and islands in the Bohai Sea, geometric fitting is essential to providing a more accurate simulation of the tidal waves and residual flow. The Bohai Sea is connected to the Yellow Sea (on the south) through the Bohai Strait. Several islands located in the Strait complicate the water exchange between these two seas. Failing to resolve these islands leads to an underestimation of water transport through the strait. It also results in an unrealistic distribution of the tidal motion in the Bohai Sea due to alterations in the propagation paths of tidal waves. In addition, in the Bohai Sea, the tidally rectified residual flow is usually one order of magnitude smaller than the buoyancy- and wind-induced flows, except near the coast and around islands. In order to obtain a more accurate simulation of temperature and salinity, the model must be able to resolve the complex topography near the coast and around islands.

In the Satilla River, the  $M_2$  tidal current accounts for about 90% of the along-river current variation (Blanton 1996). Tidal advection and mixing also are the main physical processes controlling the spatial and temporal

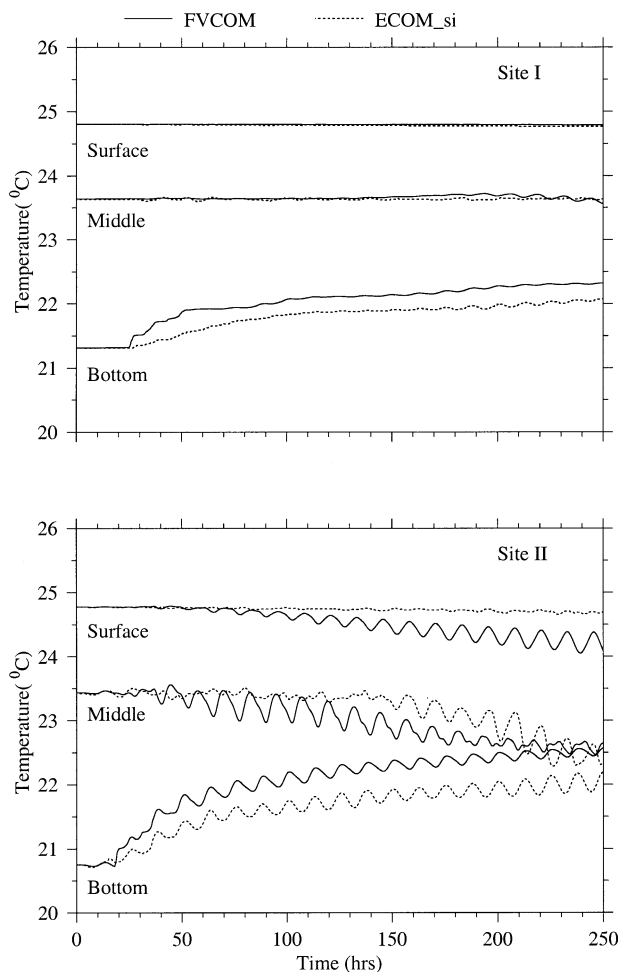


FIG. 10. Time series of model-predicted temperature at the surface ( $1/2 \sigma$  level below the surface), middle-depth, and bottom ( $1/2 \sigma$  level above the bottom) at selected sites I and II (shown in Fig. 2) in the Bohai Sea. Solid line: FVCOM; dashed line: ECOM-si.

variations of biological and chemical materials in this estuary (Bigham 1973; Dunstan and Atkinson 1976; Pomeroy et al. 1993; Verity et al. 1993; Zheng and Chen 2000). Since the Satilla River estuary features numerous tidal creeks, failing to resolve these creeks would lead to under- or overestimating the tidally rectified flow. This in turn would cause water transport in the river to be miscalculated. This can be seen clearly in the comparison between the finite-difference and finite-volume model results of the Satilla River given below.

### a. The Bohai Sea

The finite-difference model used in this comparison is ECOM-si, which is an updated version of POM. The model domains for FVCOM and ECOM-si are shown in Fig. 4, both of which have their open boundaries in the Yellow Sea about 150 km south of the Bohai Strait. In FVCOM, the horizontal resolution is about 2.6 km around the coast and about 15–20 km in the interior and

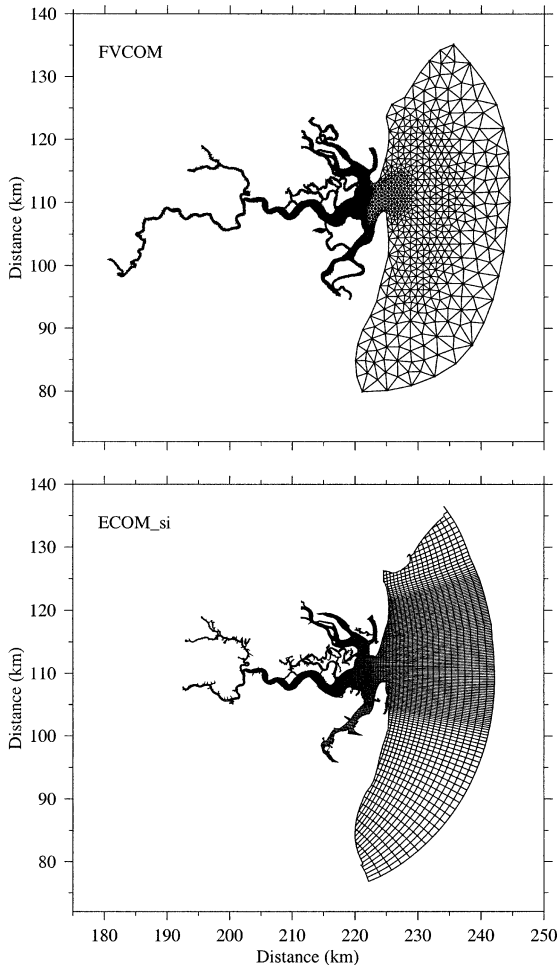


FIG. 11. Unstructured and curvilinear grids of the Satilla River for FVCOM and ECOM-si.

near the open boundary. In ECOM-si, a uniform horizontal resolution of about 2 km is used in most of the computational areas except near the open boundary where the horizontal resolution is about 7 km. In the vertical, both FVCOM and ECOM-si models comprise ten uniformly distributed  $\sigma$  layers, which result in a vertical resolution of about 0.1–1.0 m in the coastal region shallower than 10 m, and about 6 m at the 60-m isobath. The models were driven using the same semi-diurnal ( $M_2$  and  $S_2$ ) and diurnal ( $O_1$  and  $K_1$ ) tidal elevations and phases at the open boundary. The sea level data used for tidal forcing were interpolated directly from our East China/Yellow Seas model and adjusted according to previous tidal measurements at the northern and southern coasts. To examine each model's capability of simulating buoyancy-induced currents, we ran both models prognostically using the same initial stratification. The initial temperature was specified as a vertical linear function with 25°C at the surface and 15°C at a depth of 75 m. The salinity was specified as a constant

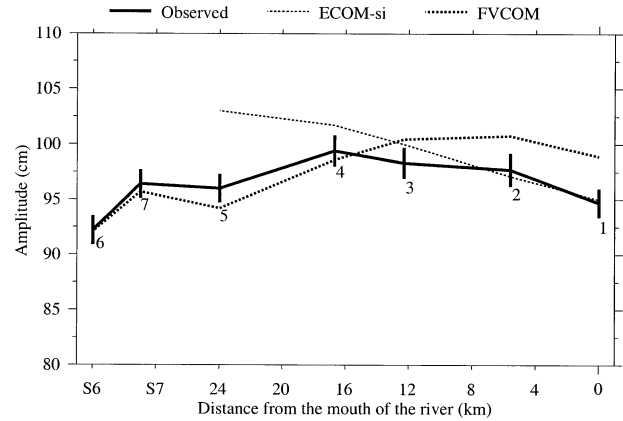


FIG. 12. Comparison between model-predicted (FVCOM and ECOM-si) and observed amplitudes of  $M_2$  tidal elevation at seven measurement sites shown in Fig. 3.

value of 30 psu. The time step was 186.3 s, which corresponded to 240 time steps over the  $M_2$  tidal cycle.

The model-predicted time series of surface elevation and currents at each grid point was fitted by a least squares harmonic analysis method. The resulting coamplitude and cophase of each tidal constituent are shown

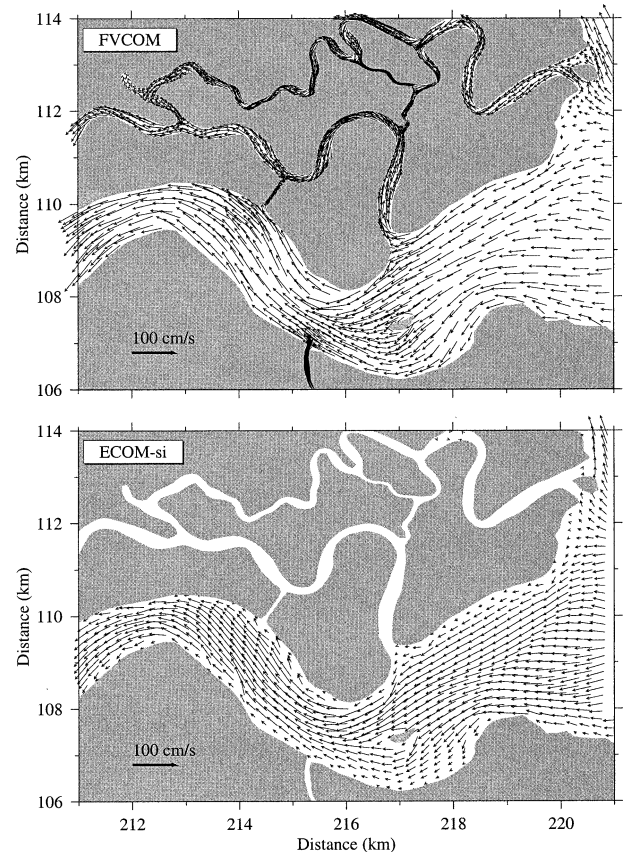


FIG. 13. Distributions of the near-surface  $M_2$  tidal currents at the maximum flood tide. (top) FVCOM and (bottom) ECOM-si.

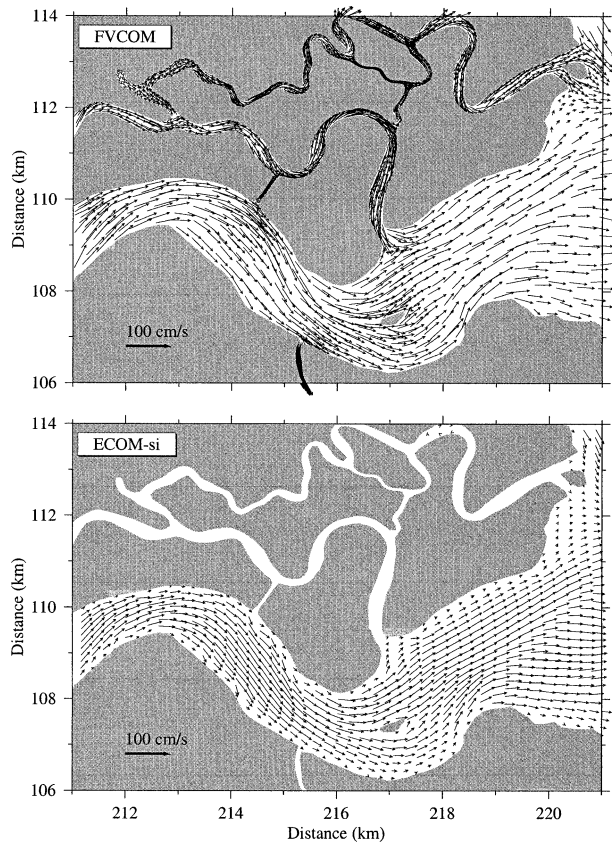


FIG. 14. Distributions of the near-surface  $M_2$  tidal currents at the maximum ebb tide. (top) FVCOM and (bottom) ECOM-si.

in Figs. 5 and 6. The model–data comparisons of tidal amplitudes and phases at tidal measurement stations are given in Tables 1–4. Although both FVCOM and ECOM-si show that  $M_2$  and  $S_2$  tidal waves propagate counterclockwise around the coast like a Kelvin wave, the distributions of tidal amplitudes and phases predicted by these two models differ significantly. FVCOM predicts two nodes of the  $M_2$  and  $S_2$  tides in the Bohai Sea: one is near the mouth of the Yellow River on the southwestern coast, and the other is located offshore of Qinhuangdao on the northwestern coast. These two nodes, however, shift onshore in the case of the ECOM-si, especially for the  $M_2$  tide. The FVCOM-predicted maximum amplitudes of the  $M_2$  and  $S_2$  tides are about 130 cm in Liaodong Bay and 100 cm in Bohai Bay, both of which are about 10–20 cm higher than those predicted by the ECOM-si. Both FVCOM and ECOM-si show similar structures for the  $K_1$  and  $O_1$  tides, but the model-predicted amplitude of the  $K_1$  tide is higher in the case with FVCOM than in the case with ECOM-si.

The comparison between observed and model-predicted amplitudes and phases of semidiurnal tides at tidal measurement stations around the Bohai Sea shows a better agreement in the case with FVCOM than in the case with ECOM-si, especially for the  $M_2$  tidal con-

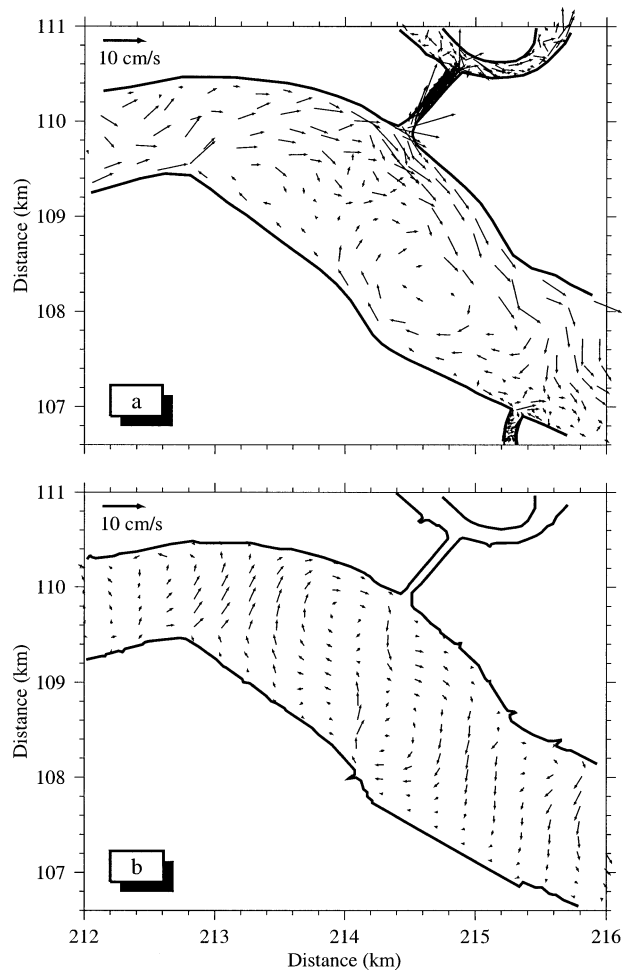


FIG. 15. Distribution of model-predicted surface residual current vectors in the selected area of the Satilla River. (top) FVCOM and (bottom) ECOM-si.

stituent in Bohai Bay and Liaodong Bay. The standard deviation for the  $M_2$  and  $S_2$  tidal simulations is 6.0 and 5.8 cm in amplitude and  $18.9^\circ$  and  $29.9^\circ$  in phase, respectively, in the case with FVCOM. However, they are 16.6 and 5.9 cm in amplitude and  $41.2^\circ$  and  $42.9^\circ$  in phase in the case with ECOM-si (Tables 1 and 2). The FVCOM is more capable of predicting the amplitude and phase of semidiurnal tides in Liaodong Bay and Bohai Bay than ECOM-si. However, no significant differences are found for the  $K_1$  and  $O_1$  tides in both the FVCOM and ECOM-si models (Tables 3 and 4).

Both FVCOM and ECOM-si predict relatively weak tidally rectified residual currents in the Bohai Sea except near the coast and around islands. In the Bohai Strait, for example, the FVCOM model shows multiple around-island residual flow patterns. These patterns are not well predicted by the ECOM-si model because of poor resolution around the islands (Fig. 7). Although both FVCOM and ECOM-si models show an eastward residual flow along the southern coast in the Bohai Sea,

TABLE 1. Model–data comparison of the  $M_2$  tidal amplitude and phase in the Bohai Sea.

Stations	Amplitude (cm)					Phase ( $^{\circ}$ G)				
	FVCOM			ECOM-si		FVCOM			ECOM-si	
	$\zeta_o$	$\zeta_c$	$\Delta\zeta$	$\zeta_c$	$\Delta\zeta$	$\phi_o$	$\phi_c$	$\Delta\phi$	$\phi_c$	$\Delta\delta$
1	88.0	89.2	-1.2	83.3	4.7	294.0	293.7	0.3	294.3	-0.3
2	83.0	80.5	2.5	79.9	3.1	300.0	301.8	-1.8	300.8	-0.8
3	59.0	53.0	6.0	54.5	4.5	350.0	351.6	-1.6	350.3	-0.3
4	61.0	57.6	3.4	60.4	0.6	11.0	9.6	1.4	14.8	-3.8
5	54.0	55.1	-1.1	56.5	-2.5	82.0	82.7	-0.7	77.5	4.5
6	71.0	73.3	-2.3	68.1	2.9	112.0	101.7	10.3	96.1	15.9
7	120.0	122.8	-2.8	112.3	7.8	125.0	125.9	-0.9	120.8	4.2
8	116.0	124.9	-8.9	107.3	8.7	145.0	145.9	-0.9	143.5	1.5
9	96.0	106.3	-10.3	82.3	13.7	150.0	155.7	-5.7	149.1	0.9
10	42.0	40.1	1.9	49.2	-7.2	153.0	164.3	-1.3	153.5	-0.5
11	25.0	28.0	-3.0	13.6	11.4	162.0	172.3	-0.3	155.2	6.8
12	13.0	20.9	-7.9	6.1	6.9	170.0	185.2	-5.2	159.2	10.8
13	12.0	15.6	-3.6	6.1	5.9	179.0	192.6	-3.6	159.2	19.8
14	5.0	11.1	-6.1	11.4	-6.4	282.0	269.4	12.6	332.0	-50.0
15	11.0	15.6	-4.6	17.8	-6.8	311.0	291.8	19.2	337.2	-26.2
16	17.0	22.5	-5.5	24.5	-7.5	339.0	317.5	21.5	343.1	-4.1
17	32.0	31.5	0.5	24.5	7.5	0.0	341.4	18.6	343.1	16.9
18	73.0	66.2	6.8	54.1	18.9	74.0	67.2	6.8	66.8	7.2
19	12.10	106.1	14.9	77.1	43.9	85.0	80.7	4.3	79.8	5.2
20	117.0	111.2	5.8	77.1	39.9	90.0	86.3	3.7	79.8	10.2
21	106.0	117.1	-11.1	94.9	11.1	96.0	99.6	-3.6	116.4	-20.4
22	112.0	106.6	5.4	94.9	17.1	109.0	110.2	-1.2	116.4	-7.4
23	84.0	75.5	8.5	56.1	27.9	127.0	114.1	12.9	130.4	-3.4
24	49.0	50.9	-1.9	30.0	19.0	313.0	322.1	-9.1	124.3	-71.3
25	46.0	50.3	-4.3	58.5	-12.5	230.0	322.2	-2.2	353.7	-23.7
26	48.0	50.4	-2.4	54.0	-6.0	320.0	330.2	-0.2	3.4	-43.4
27	51.0	45.5	5.5	40.8	10.2	319.0	335.0	-6.0	3.2	-44.2
28	40.0	32.4	7.6	22.5	17.5	316.0	324.0	-8.0	340.4	-24.4
29	60.0	55.1	4.9	49.3	10.7	300.0	300.5	-0.5	297.4	2.6
30	54.0	47.9	6.1	43.1	10.9	296.0	296.6	-0.6	294.4	1.6
31	74.0	69.7	4.3	32.2	41.8	290.0	283.4	6.6	282.1	7.9
32	76.0	74.1	1.9	73.9	2.1	290.0	284.6	5.4	277.4	12.6
Std dev			6.0		16.6			18.9		41.2

Note:  $\zeta_o$ —observed amplitude;  $\zeta_c$ —computed amplitude;  $\Delta\zeta = \zeta_o - \zeta_c$ ;  $\phi_o$ —observed phase;  $\phi_c$ —computed phase; and  $\Delta\phi = \phi_o - \phi_c$ .

the current is trapped near the coast and is much stronger in the case with FVCOM than in the case with ECOM-si. Similar disparities also are found around the islands in the eastern coast and Bohai Bay.

For the same initial distribution of temperature, the distributions of the temperature predicted by FVCOM and ECOM-si on the 10th model day are similar in the interior but differ significantly around the coast and islands. In the horizontal, both models predict a tidal mixing front around the 15-m isobath and a relatively uniform temperature in the interior (Fig. 8). In the vertical, they also show the similar tidal mixing height above the bottom on sections 1 and 2 (Fig. 9). The major difference is that the cross-frontal gradient of temperature around the 15-m isobath is relatively larger in the case with FVCOM than in the case with ECOM-si. Also, the model-predicted depth of the thermocline in section 1 is shallower in the case with FVCOM than in the case with ECOM-si.

Disparity in the field of the temperature between FVCOM and ECOM-si is believed due to the difference of the accuracy of geometric matching between these

two models. At site I (in the interior), for example, both FVCOM and ECOM-si show that the temperature at the surface and middle depth remains almost unchanged during the first 10 model days, while the temperature near the bottom starts mixing up after 1 day (the model boundary forcing is ramped up from zero to full amplitude over the first 24 h of model integration) and reaches to an equilibrium state after 4 model days (Fig. 10a). FVCOM shows relatively stronger mixing on the second model day, which probably is caused by the difference in horizontal resolution and water depth interpolated from irregularly distributed dataset between these two models. At site 2 (around an island close to the Bohai Strait), the near-surface temperature decreases slightly with time in the case with ECOM-si, but drops more rapidly with time and also oscillates periodically after the fourth model day in the case with FVCOM (Fig. 10b). Although temperature at middle depth and near the bottom predicted by these two models tends to mix up after 10 model days, the mixing rate seems faster in FVCOM than in ECOM-si (Fig. 10b).

This is not a surprising result since the topography

TABLE 2. Model–data comparison of the  $S_2$  tidal amplitude and phase in the Bohai Sea.

Stations	Amplitude (cm)					Phase ( $^{\circ}$ G)				
	FVCOM			ECOM-si		FVCOM			ECOM-si	
	$\zeta_o$	$\zeta_c$	$\Delta\zeta$	$\zeta_c$	$\Delta\zeta$	$\phi_o$	$\phi_c$	$\Delta\phi$	$\phi_c$	$\Delta\phi$
1	26.0	17.6	8.4	27.1	-1.1	348.0	349.7	-1.7	344.6	3.4
2	25.0	15.6	9.4	25.6	-0.6	355.0	358.7	-3.7	351.2	3.8
3	18.0	10.0	8.0	17.9	0.1	48.0	46.6	1.4	42.3	5.7
4	21.0	10.8	10.2	19.6	1.4	69.0	63.5	5.5	65.9	3.1
5	15.0	9.0	6.0	17.4	-2.4	139.0	144.5	-5.5	135.5	3.5
6	19.0	13.6	5.4	21.4	-2.4	167.0	166.5	0.5	156.3	10.7
7	37.0	25.9	11.1	38.1	-1.1	188.0	190.4	-2.4	180.5	7.5
8	32.0	26.1	5.9	36.8	-4.8	209.0	211.2	-2.2	203.7	5.3
9	27.0	20.7	6.3	27.6	-0.6	210.0	222.3	-12.3	212.5	-2.5
10	11.0	5.2	5.8	15.5	-4.5	216.0	243.9	-27.9	221.0	-5.0
11	5.0	2.6	2.4	3.7	1.3	205.0	263.7	-58.7	253.7	-48.7
12	2.0	1.5	0.5	2.3	-0.3	227.0	291.0	-64.0	300.7	-73.7
13	2.0	1.2	0.8	2.3	-0.3	203.0	310.5	-107.5	300.7	-97.7
14	1.0	3.0	-2.0	6.5	-5.5	39.0	4.1	34.9	18.0	21.0
15	5.0	4.4	0.6	8.6	-3.6	37.0	15.7	21.3	27.3	9.7
16	5.0	6.2	-1.2	10.8	-5.8	33.0	30.9	2.1	36.6	-3.6
17	11.0	7.8	3.2	10.8	0.2	65.0	51.4	13.6	36.6	28.4
18	20.0	17.6	2.4	20.4	-0.4	148.0	142.4	5.6	135.0	13.0
19	34.0	32.3	1.7	31.0	3.0	159.0	154.1	4.9	147.7	11.3
20	34.0	34.1	-0.1	31.0	3.0	165.0	161.3	3.7	147.7	17.3
21	30.0	36.4	-6.4	40.5	-10.5	177.0	174.2	2.8	182.2	-5.2
22	32.0	32.5	-0.5	40.5	-8.5	186.0	186.7	-0.7	182.2	3.8
23	24.0	21.8	2.3	22.4	1.6	196.0	194.5	1.5	203.2	-7.2
24	17.0	19.8	-2.8	10.8	6.2	45.0	23.0	22.0	204.1	-159.1
25	9.0	19.4	-10.4	30.2	-21.2	307.0	23.3	-76.3	57.7	-110.7
26	16.0	19.3	-3.3	27.7	-11.7	46.0	32.8	13.2	68.9	-22.9
27	18.0	16.9	1.1	20.4	-2.4	48.0	38.8	9.2	70.8	-22.8
28	13.0	10.3	2.7	9.6	3.4	38.0	35.0	3.0	54.6	-16.6
29	18.0	10.7	7.3	16.7	1.3	3.0	1.9	1.1	351.3	11.7
30	17.0	9.6	7.4	14.7	2.3	358.0	2.2	-4.2	351.0	7.0
31	21.0	14.0	7.0	10.4	10.6	351.0	345.4	5.6	338.5	12.5
32	22.0	15.9	6.1	26.3	-4.3	345.0	347.5	-2.5	336.3	8.7
Std dev			5.8		5.9			29.9		42.9

Note:  $\zeta_o$ —observed amplitude;  $\zeta_c$ —computed amplitude;  $\Delta\zeta = \zeta_o - \zeta_c$ ;  $\phi_o$ —observed phase;  $\phi_c$ —computed phase; and  $\Delta\phi = \phi_o - \phi_c$ .

around the island is resolved well in FVCOM but not in ECOM-si. If we believe that both FVCOM and ECOM-si have the same numerical accuracy, then we could conclude here that poor matching of the complex coastal geometries in the finite-difference model would underestimate mixing around the coast, which would eventually lead to the unrealistic distribution of the temperature in the interior, especially in a semienlosed coastal ocean like the Bohai Sea. Also, we learn from site 2 that the mismatch in the island geometry would filter a relatively large tidal oscillation near the surface, which tends to produce significant mixing near the surface under conditions with no heat flux.

#### b. The Satilla River

The model grids of FVCOM and ECOM-si for the Satilla River are shown in Fig. 11. The horizontal resolution of ECOM-si is 100 m in the main channel of the river and up to 2500 m near the open boundary in the inner shelf. Similar sizes of unstructured grids are used in FVCOM. In both models, the vertical is divided

into 10 uniform  $\sigma$  layers, which correspond to a vertical resolution of less than 0.5 m in most areas inside the river. The models were driven by the same semidiurnal  $M_2$  tidal forcing at the open boundary. The harmonic constants of the  $M_2$  tidal forcing were specified using the tidal elevations and phases predicted by the inner shelf South Atlantic Bight (SAB) tidal model [developed and calibrated by Chen et al. (1999)]. No stratification or river discharge is included in this model comparison experiment.

The model results show a significant difference in the along-river distribution of the  $M_2$  tidal amplitude between FVCOM and ECOM-si (Fig. 12). The observed amplitude of the  $M_2$  tidal constituent is  $94.7 \pm 1.3$  cm at site 1, gradually increases to  $99.4 \pm 1.4$  cm at site 4, and then decreases to  $96.0 \pm 1.3$  cm at site 5. At sites 6 and 7 in the southern and northern branches separated at the upstream end of the main river channel, the observed amplitudes are  $92.2 \pm 1.3$  cm and  $96.4 \pm 1.3$  cm, respectively. The amplitude of the sea level predicted by ECOM-si increases upstream, with values significantly higher than the observed values at sites 4

TABLE 3. Model–data comparison of the  $K_1$  tidal amplitude and phase in the Bohai Sea.

Stations	Amplitude (cm)					Phase (°G)				
	FVCOM			ECOM-si		FVCOM			ECOM-si	
	$\zeta_o$	$\zeta_c$	$\Delta\zeta$	$\zeta_c$	$\Delta\zeta$	$\phi_o$	$\phi_c$	$\Delta\phi$	$\phi_c$	$\Delta\phi$
1	22.0	23.0	-1.0	19.1	2.9	7.0	0.9	6.1	5.4	1.6
2	22.0	20.5	1.5	18.6	3.4	14.0	10.8	3.2	11.9	2.1
3	24.0	22.9	1.1	20.3	3.7	57.0	54.9	2.1	49.6	7.4
4	30.0	26.0	4.0	23.7	6.3	68.0	60.5	7.5	58.1	9.9
5	33.0	32.2	0.8	28.4	4.6	81.0	75.9	5.1	74.2	6.8
6	39.0	34.9	4.1	30.2	8.8	95.0	79.0	16.0	78.4	16.6
7	43.0	40.2	2.8	35.2	7.8	85.0	84.4	0.6	83.2	1.8
8	38.0	40.6	-2.6	35.2	2.8	100.0	93.5	6.5	93.6	6.4
9	38.0	39.1	-1.1	33.2	4.8	104.0	98.1	5.9	98.0	6.0
10	35.0	33.3	1.7	30.2	4.8	107.0	102.3	4.7	101.1	5.9
11	33.0	32.3	0.7	26.9	6.1	91.0	103.7	-12.7	103.8	-12.8
12	37.0	31.7	5.3	26.2	10.8	107.0	105.1	1.9	105.1	1.9
13	32.0	31.3	0.7	26.2	5.8	95.0	105.8	-10.8	105.1	-10.1
14	29.0	30.6	-1.6	25.2	3.8	108.0	109.9	-1.9	110.1	-2.1
15	29.0	30.7	-1.7	25.0	4.0	111.0	112.2	-1.2	112.9	-1.9
16	28.0	30.5	-2.5	24.9	3.1	114.0	116.3	-2.3	117.1	-3.1
17	28.0	29.7	-1.7	24.9	3.1	127.0	122.7	4.3	117.1	9.9
18	31.0	34.2	-3.2	26.4	4.6	153.0	145.8	7.2	147.0	6.0
19	42.0	39.1	2.9	29.4	12.6	154.0	146.9	7.1	147.4	6.6
20	36.0	40.0	-4.0	29.4	6.6	154.0	149.6	4.4	147.4	6.6
21	28.0	40.9	-12.9	32.1	-4.1	140.0	154.8	-14.8	159.9	-19.9
22	38.0	40.3	-2.3	32.1	5.9	161.0	160.3	0.7	159.9	1.1
23	29.0	37.3	-8.3	28.8	0.2	174.0	164.4	9.6	170.2	3.8
24	27.0	32.1	-5.1	25.8	1.2	197.0	187.3	9.7	171.1	25.9
25	18.0	31.8	-13.8	23.0	-5.0	180.0	187.5	-7.5	196.0	-16.0
26	25.0	31.5	-6.5	22.5	2.5	194.0	193.2	0.8	202.8	-8.8
27	22.0	30.4	-8.4	20.6	1.4	197.0	197.1	-0.1	206.7	-9.7
28	20.0	25.5	-5.5	17.3	2.7	200.0	203.9	-3.9	214.5	-14.5
29	7.0	3.6	3.4	3.7	3.3	17.0	338.3	38.7	345.2	31.8
30	1.0	6.7	-5.7	5.2	-4.2	179.0	242.7	-63.7	258.5	-79.5
31	15.0	18.4	-3.4	14.1	0.9	281.0	277.4	3.6	239.2	41.8
32	16.0	21.3	-5.3	16.8	-0.8	295.0	295.3	-0.3	288.5	6.5
Std dev			5.1		5.2			14.8		19.3

Note:  $\zeta_o$ —observed amplitude;  $\zeta_c$ —computed amplitude;  $\Delta\zeta = \zeta_o - \zeta_c$ ;  $\phi_o$ —observed phase;  $\phi_c$ —computed phase; and  $\Delta\phi = \phi_o - \phi_c$ .

and 5. Since ECOM-si fails to resolve the two river branches at the upstream end of the main channel, water flooding up the river tends to accumulate there. In contrast, FVCOM not only predicts the same trend of the  $M_2$  tidal amplitude as the observations from site 4 to 7, but also their values agree with each other within measurement uncertainty. In addition, FVCOM shows higher values of the amplitude than the observations at sites 1–3, which is believed due to the flooding/drying process over the intertidal zone around the mouth of the river.

Zheng et al. (2002b) incorporated a 3D wet/dry point treatment method into ECOM-si and used it to simulate the amplitude and phase of the  $M_2$  tidal constituent in the Satilla River. They found that the flooding/drying process plays a key role in simulating tidal elevation and currents in the main river channel. Including the intertidal zone in the ECOM-si did show a significant improvement in the simulation of tidal elevation at site 5, but it still fails to provide reasonable values of the amplitude at sites 6 and 7. To make the model-predicted tidal elevation match the observed value at measurement

sites, Zheng et al. (2002b) tuned the model by adjusting the bottom roughness  $z_o$ . Since we have not yet added flooding/drying to FVCOM, the model comparison made is between both models without this process.

Tidal currents computed by FVCOM and ECOM-si also differ significantly, especially around the estuary–tidal creek area (Figs. 13 and 14). FVCOM shows a relatively strong tidal current near both the southern and northern coasts, with a substantial inflow to and outflow from tidal creeks during flood and ebb tides, respectively. These patterns are not resolved in ECOM-si. FVCOM predicts a stronger along-coast residual flow near the tidal creek, which intensifies the topographically induced eddylike residual circulation cell on the eastern side of the tidal creek (Fig. 15a). Although this eddylike residual circulation cell is also predicted in ECOM-si, it is much weaker and the velocity is symmetrically distributed relative to its center (Fig. 15b).

### 6. Discussion and summary

An unstructured grid, finite-volume, three-dimensional primitive equation coastal ocean model

TABLE 4. Model–data comparison of the  $O_1$  tidal amplitude and phase in the Bohai Sea.

Stations	Amplitude (cm)					Phase ( $^{\circ}$ G)				
	FVCOM			ECOM-si		FVCOM			ECOM-si	
	$\zeta_o$	$\zeta_c$	$\Delta\zeta$	$\zeta_c$	$\Delta\zeta$	$\phi_o$	$\phi_c$	$\Delta\phi$	$\phi_c$	$\Delta\phi$
1	17.0	15.2	1.8	16.2	0.8	328.0	319.0	9.0	327.8	0.2
2	16.0	13.7	2.3	16.0	0.0	334.0	331.7	2.3	334.9	-0.9
3	19.0	17.7	1.3	18.9	0.1	10.0	13.9	-3.9	12.9	-2.9
4	23.0	20.0	3.0	22.0	1.0	17.0	17.9	-0.9	20.4	-3.4
5	25.0	24.6	0.4	26.4	-1.4	32.0	30.3	1.7	35.0	-3.0
6	27.0	26.4	0.6	28.1	-1.1	45.0	32.8	12.2	38.7	6.3
7	30.0	29.8	0.2	32.2	-2.2	46.0	37.3	8.7	42.9	3.1
8	26.0	30.0	-4.0	32.8	-6.8	47.0	45.6	1.4	52.5	-5.5
9	29.0	29.1	-0.1	31.4	-2.4	54.0	49.9	4.1	56.5	-2.5
10	26.0	25.6	0.4	29.2	-3.2	50.0	53.9	-3.9	59.2	-9.2
11	25.0	25.0	0.0	26.7	-1.7	53.0	55.2	-2.2	61.5	-8.5
12	26.0	24.6	1.4	26.2	-0.2	52.0	56.3	-4.3	62.6	-10.6
13	23.0	24.4	-1.4	26.2	-3.2	52.0	57.0	-5.0	62.6	-10.6
14	27.0	24.1	2.9	25.6	1.4	61.0	60.5	0.5	66.6	-5.6
15	23.0	24.2	-1.2	25.7	-2.7	61.0	62.3	-1.3	68.9	-7.9
16	25.0	24.2	0.8	25.7	-0.7	67.0	65.8	1.2	72.2	-5.2
17	24.0	23.8	0.2	25.7	-1.7	69.0	71.2	-2.2	72.2	-3.2
18	25.0	27.1	-2.1	27.8	-2.8	94.0	89.9	4.1	95.4	-1.4
19	30.0	30.5	-0.5	30.5	-0.5	96.0	90.4	5.6	95.5	0.5
20	27.0	31.1	-4.1	30.5	-3.5	99.0	92.8	6.2	95.5	3.5
21	18.0	31.7	-13.7	32.7	-14.7	103.0	97.4	5.6	105.8	-2.8
22	31.0	31.4	-0.4	32.7	-1.7	111.0	102.6	8.4	105.8	5.2
23	27.0	29.4	-2.4	29.6	-2.6	116.0	106.7	9.3	114.5	1.5
24	24.0	26.0	-2.0	26.9	-2.9	132.0	126.6	5.4	115.4	16.6
25	12.0	25.8	-13.8	23.6	-11.6	132.0	126.9	5.1	136.0	-4.0
26	26.0	25.6	0.4	22.9	3.1	138.0	132.2	5.8	142.2	-4.2
27	23.0	24.8	-1.8	21.2	1.8	132.0	135.8	-3.8	145.8	-13.8
28	17.0	21.2	-4.2	17.8	-0.8	138.0	141.8	-3.8	152.7	-14.7
29	4.0	1.3	2.7	1.7	2.3	12.0	68.1	-56.1	4.3	7.7
30	3.0	6.0	-3.0	4.3	-1.3	63.0	151.7	-88.7	170.8	-107.8
31	9.0	12.3	-3.3	13.5	-4.5	232.0	206.2	25.8	175.5	56.5
32	9.0	13.4	-4.4	14.0	-5.0	234.0	225.7	8.3	240.5	-6.5
Std dev			4.0		4.1			19.8		22.6

Note:  $\zeta_o$ —observed amplitude;  $\zeta_c$ —computed amplitude;  $\Delta\zeta = \zeta_o - \zeta_c$ ;  $\phi_o$ —observed phase;  $\phi_c$ —computed phase; and  $\Delta\phi = \phi_o - \phi_c$ .

(FVCOM) has been developed for the study of coastal and estuarine circulation. This model combines the advantages of the finite-element method for geometric flexibility and finite-difference method for simple discrete computational efficiency. The numerical experiments in the Bohai Sea and Satilla River demonstrate that this model provides a more accurate simulation of tidal currents and residual flow in coastal ocean and estuarine settings where multiple islands, inlets, and tidal creeks exist. Because of a better fitting of the geometric complex in FVCOM, this model should provide a more accurate representation of water mass property variability and the advection and mixing of passive tracers around the coast.

FVCOM and ECOM-si show similar accuracy in the tracer simulation experiments except around complex topographies. Regarding the finite-difference approach, the most significant improvement provided by FVCOM is the geometric flexibility with unstructured grids. Recently, some model experiments were conducted with FVCOM, ECOM-si, and POM for two idealized cases with analytic solutions: free long gravity waves in a

circular lake, and tidal wave resonance in a simple semi-enclosed channel. The results show in the first case that poor resolution of the curved coastal geometry causes both unwanted wave damping and a time-dependent phase shift. In the second case, the near-resonance behavior is strongly influenced by channel shape irregularities. This may explain why FVCOM provides a more accurate simulation for the amplitude of the  $M_2$  tidal constituent in Bohai Bay. A manuscript describing these and other idealized model comparisons is in preparation.

The goal of this paper is to introduce the unstructured grid, finite-volume numerical approach to the coastal ocean community. We fully understand that more experiments and comparisons with analytical solutions and other models must be made in order to validate the usefulness and reliability of this new finite-volume ocean model for the study of coastal and estuarine circulation and ecosystem dynamics.

Recently, a wet/dry point treatment technique was introduced into FVCOM. It is now being tested in the Satilla River, an estuary characterized by intensive intertidal salt marshes. Also, a Lagrangian particle track-

ing code was added into the FVCOM code, and is being tested through comparison with ECOM-si. Water quality and suspended sediment models are also being developed. The formulations of these models are the same as the water quality and suspended sediment models we developed for Georgia estuaries based on ECOM-si (Zheng et al. 2002a). Hopefully, as FVCOM matures, others will join in our efforts to make this an important tool to better understand our coastal environment.

*Acknowledgments.* This research was supported by the Georgia Sea Grant College Program under Grants NA26RG0373 and NA66RG0282, the National Science Foundation under Grant OCE-97-12869, and the U.S. GLOBEC Georges Bank Program through support from NOAA Grants NA56RG0487, NA96OP003, and NA96OP005 and NSF Grant OCE 98-06379. We want to especially thank M. Rawson, manager of the Georgia Sea Grant College Program, for his strong encouragement and support of this model development effort. Without the continuous financial support of the Georgia Sea Grant College Program, this model development would not have been possible. We also want to thank A. Blumberg, who gave us permission to use ECOM-si during the last 10 years. Our experience with ECOM-si has helped us build a solid foundation in modeling, which in turn has directly benefited us in developing FVCOM. G. Davidson (Georgia Sea Grant College Program) provided editorial help on this manuscript. His assistance is greatly appreciated. Three anonymous reviewers provided many critical comments and constructive suggestions, which really helped us to improve the model–data comparison and clarify the final manuscript.

APPENDIX

The Discrete Form of the 2D External and 3D Internal Modes

a. The 2D external mode

In the 2D external mode equations  $R_u^n$  and  $R_v^n$  are expressed by

$$R_u^n = ADVU + DPBPX + DPBCX + CORX + VISCX - G_x, \tag{A.1}$$

$$R_v^n = ADVV + DPBPY + DPBCY + CORY + VISCY - G_y, \tag{A.2}$$

where  $ADVU$  and  $ADVV$ ,  $DPBPX$  and  $DPBPY$ ,  $DPBCX$  and  $DPBCY$ ,  $CORX$  and  $CORY$ ,  $VISCX$  and  $VISCY$  are the  $x$  and  $y$  components of vertically integrated horizontal advection, barotropic pressure gradient force, Coriolis force, and horizontal diffusion terms, respectively. The definitions of  $G_x$  and  $G_y$  are the same as those shown in Eqs. (2.40) and (2.41) in the text.

The  $x$  and  $y$  components of the horizontal advection are calculated numerically by

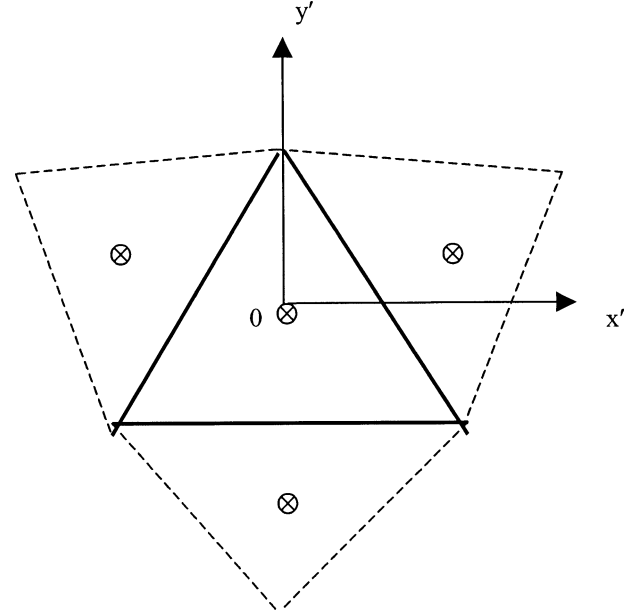


FIG. A1. The illustration of the local coordinates.

$$ADVU = \sum_{m=1}^3 (\bar{u}_{im} \bar{D}_m \cdot \bar{v}_{nm} \hat{l}_m),$$

$$ADVV = \sum_{m=1}^3 (\bar{v}_{im} \bar{D}_m \cdot \bar{v}_{nm} \hat{l}_m), \tag{A.3}$$

where  $\bar{u}_{im}$ ,  $\bar{v}_{im}$ , and  $\bar{v}_{nm}$  are the  $x$ ,  $y$ , and normal components of the velocity on the side line  $m$  of a triangle cell, and  $\bar{v}_{nm}$  is positive when its direction is outward. Here  $\hat{l}_m$  and  $\bar{D}_m$  are the length and midpoint water depth of the side line  $m$ , respectively. They are equal to

$$\bar{D}_m = 0.5[D(N_i(j_1)) + D(N_i(j_2))] \tag{A.4}$$

$$\hat{l}_m = \{[X_n(N_i(j_1)) - X_n(N_i(j_2))]^2 + [Y_n(N_i(j_1)) - Y_n(N_i(j_2))]^2\}^{1/2}, \tag{A.5}$$

where

$$j_2 = m + 1 - \text{INT}\left(\frac{m+1}{4}\right) \times 3;$$

$$j_1 = m + 2 - \text{INT}\left(\frac{m+2}{4}\right) \times 3. \tag{A.6}$$

The velocity in the triangle cell  $i$  is assumed to satisfy the linear distribution given as

$$\bar{u}_i(x', y') = \phi_i^u(x', y') = \bar{u}_{i,0} + a_i^u x' + b_i^u y', \tag{A.7}$$

$$\bar{v}_i(x', y') = \phi_i^v(x', y') = \bar{v}_{i,0} + a_i^v x' + b_i^v y', \tag{A.8}$$

where the parameters  $a_i^u$ ,  $b_i^u$ ,  $a_i^v$ , and  $b_i^v$  are determined by a least squares method based on velocity values at the four cell centered points shown in Fig. A1 (one calculated cell plus three surrounding cells). Then, the normal velocity component on the side line  $m$  is given as

$$\bar{v}_{nm} = \hat{v}_m \cos\theta - \hat{u}_m \sin\theta, \quad (\text{A.9}) \quad DPBCX$$

where

$$\theta = \arctan \frac{Y_n(N_i(j_2)) - Y_n(N_i(j_1))}{X_n(N_i(j_2)) - X_n(N_i(j_1))}, \quad \text{and} \quad (\text{A.10})$$

$$\hat{u}_{im} = 0.5[\phi_i^u(\bar{x}'_m, \bar{y}'_m) + \phi_{NB_i(m)}^u(\bar{x}'_m, \bar{y}'_m)],$$

$$\hat{v}_{im} = 0.5[\phi_i^v(\bar{x}'_m, \bar{y}'_m) + \phi_{NB_i(m)}^v(\bar{x}'_m, \bar{y}'_m)], \quad (\text{A.11})$$

where  $\bar{x}'_m$  and  $\bar{y}'_m$  are the midpoint of the side line  $m$ .

The momentum flux through three side sections of triangle cell  $i$  is calculated using a second-order accuracy (Kobayashi et al. 1999; Hubbard 1999) as follows:

$$\bar{u}_{im} = \begin{cases} \phi_i^u(0, 0), & \bar{v}_{nm} < 0 \\ \phi_{NB_i(m)}^u(x_{im}, y_{im}), & \bar{v}_{nm} \geq 0, \end{cases}$$

$$\bar{v}_{im} = \begin{cases} \phi_i^v(0, 0), & \bar{v}_{nm} < 0 \\ \phi_{NB_i(m)}^v(x_{im}, y_{im}), & \bar{v}_{nm} \geq 0, \end{cases} \quad (\text{A.12})$$

where  $x_{im}$  and  $y_{im}$  are the cell-centered point of the surrounding triangle numbered  $NB_i(m)$ , and  $(0, 0)$  indicates the location of the cell-centered point.

The area integration of barotropic pressure gradient force terms can be converted to a trajectory integration using Stokes' theorem. They can then be calculated numerically by a simple discrete method as follows:

$$DPBPX = g\bar{D}_i \sum_{m=1}^3 \bar{\zeta}_m [Y_n(N_i(j_1)) - Y_n(N_i(j_2))], \quad (\text{A.13})$$

$$DPBPY = g\bar{D}_i \sum_{m=1}^3 \bar{\zeta}_m [X_n(N_i(j_2)) - X_n(N_i(j_1))], \quad (\text{A.14})$$

where  $\bar{\zeta}_m = 0.5[\zeta(N_i(j_1)) + \zeta(N_i(j_2))]$ .

A similar approach is used to calculate the baroclinic pressure gradient force terms. These terms are rewritten into the form of the gradient to take the advantage of the flux calculation in the finite-volume method. For example, the  $x$  component of the baroclinic pressure gradient force can be rewritten as

$$-\frac{gD}{\rho_o} \left[ \frac{\partial}{\partial x} \left( D \int_{\sigma}^0 \rho d\sigma' \right) + \sigma \rho \frac{\partial D}{\partial x} \right]$$

$$= -\frac{gD}{\rho_o} \left\{ \frac{\partial}{\partial x} \left[ D \int_{\sigma}^0 \rho d\sigma + \sigma \rho D \right] - D \frac{\partial \rho \sigma}{\partial x} \right\}$$

$$= \frac{gD}{\rho_o} \left\{ \frac{\partial}{\partial x} D \int_{\sigma}^0 \sigma \frac{\partial \rho}{\partial \sigma} d\sigma + D \frac{\partial \rho \sigma}{\partial x} \right\}. \quad (\text{A.15})$$

Integrating Eq. (A.15) from  $-1$  to  $0$  and then integrating over a triangle cell area again, we get

$$= \frac{g}{\rho_o} \left\{ \iiint \left[ D \frac{\partial}{\partial x} \int_{-1}^0 \left( D \int_{\sigma}^0 \rho \frac{\partial \rho}{\partial \sigma'} d\sigma' \right) d\sigma \right] dx dy \right.$$

$$\left. + \iint D^2 \frac{\partial}{\partial x} \left( \int_{-1}^0 \rho \sigma d\sigma \right) dx dy \right\}$$

$$= \frac{g}{\rho_o} \left\{ \bar{D} \oint \left[ D \int_{-1}^0 \left( \int_{\sigma}^0 \sigma \frac{\partial \rho}{\partial \sigma'} d\sigma' \right) d\sigma \right] dy \right.$$

$$\left. + \bar{D}^2 \oint \left( \int_{-1}^0 \rho \sigma d\sigma \right) dy \right\}. \quad (\text{A.16})$$

The discrete form of Eq. (A.16) is given as

$$DPBCX = \frac{0.5g}{\rho_o} \left\{ \bar{D}_i \sum_{m=1}^3 \bar{D}_m [PB_1(i) + PB_2(NB_i(m))] \right.$$

$$\times [Y_n(N_i(j_1)) - Y_n(N_i(j_2))]$$

$$+ \bar{D}_i^2 \sum_{m=1}^3 [PB_2(i) - PB_2(NB_i(m))]$$

$$\left. \times [Y_n(N_i(j_1)) - Y_n(N_i(j_2))] \right\}, \quad (\text{A.17})$$

where

$$PB_1(i) = \sum_{k'=1}^{KB-1} \left\{ [\sigma(k') - \sigma(k'+1)] \right.$$

$$\left. \times \sum_{k=1}^{k'} \sigma(k) [\rho(k) - \rho(k+1)] \right\} \quad (\text{A.18})$$

$$PB_2(i) = 0.5 \sum_{k'=1}^{KB-1} [\rho(k) + \rho(k+1)]$$

$$\times \sigma(k) [\sigma(k) - \sigma(k+1)]. \quad (\text{A.19})$$

Similarly, we can derive the  $y$  component of the baroclinic pressure gradient force as

$$DPBCY = \frac{0.5g}{\rho_o} \left\{ \bar{D}_i \sum_{m=1}^3 \bar{D}_m [PB_1(i) + PB_2(NB_i(m))] \right.$$

$$\times [X_n(N_i(j_2)) - X_n(N_i(j_1))]$$

$$+ \bar{D}_i^2 \sum_{m=1}^3 [PB_2(i) + PB_2(NB_i(m))]$$

$$\left. \times [X_n(N_i(j_2)) - X_n(N_i(j_1))] \right\}. \quad (\text{A.20})$$

The discrete forms of the Coriolis force terms are given as

$$CORX = -fv_i D_i \Omega_i^u; \quad CORY = fu_i D_i \Omega_i^v. \quad (\text{A.21})$$

The  $x$  and  $y$  components of the horizontal diffusion can be rewritten as

$$\begin{aligned} \iint D\tilde{F}_x \, dx \, dy &\approx \iint \left\{ \frac{\partial}{\partial x} \left( 2\bar{A}_m H \frac{\partial \bar{u}}{\partial x} \right) + \frac{\partial}{\partial y} \left[ \bar{A}_m H \left( \frac{\partial \bar{u}}{\partial y} + \frac{\partial \bar{v}}{\partial x} \right) \right] \right\} dx \, dy \\ &= 2 \oint \bar{A}_m H \frac{\partial \bar{u}}{\partial x} \, dy - \oint \bar{A}_m H \left( \frac{\partial \bar{u}}{\partial y} + \frac{\partial \bar{v}}{\partial x} \right) dx \quad \text{and} \end{aligned} \tag{A.22}$$

$$\begin{aligned} \iint D\tilde{F}_y \, dx \, dy &\approx \iint \left\{ \frac{\partial}{\partial y} \left( 2\bar{A}_m H \frac{\partial \bar{v}}{\partial y} \right) + \frac{\partial}{\partial x} \left[ \bar{A}_m H \left( \frac{\partial \bar{u}}{\partial y} + \frac{\partial \bar{v}}{\partial x} \right) \right] \right\} dx \, dy \\ &= -2 \oint \bar{A}_m H \frac{\partial \bar{v}}{\partial y} \, dx + \oint \bar{A}_m H \left( \frac{\partial \bar{u}}{\partial y} + \frac{\partial \bar{v}}{\partial x} \right) dy. \end{aligned} \tag{A.23}$$

The discrete forms of Eqs. (A.22) and (A.23) are given as

$$\begin{aligned} VISCX = \sum_{m=1}^3 \left\{ 0.5\bar{H}_m [\bar{A}_m(i) + \bar{A}_m(NB(m))] [a^u(i) + a^u(NB(m))] [Y_n(N_i(j_1)) - Y_n(N_i(j_2))] \right. \\ \left. + 0.25\bar{H}_m [\bar{A}_m(i) + \bar{A}_m(NB(m))] [b^u(i) + b^u(NB(m)) + a^v(i) + a^v(NB(m))] \right. \\ \left. [X_n(N_i(j_2)) - X_n(N_i(j_1))] \right\}, \end{aligned} \tag{A.24}$$

where  $\bar{H}_m = 0.5[H(N_i(j_1)) + H(N_i(j_2))]$ , and

$$\begin{aligned} VISCY = \sum_{m=1}^3 \left\{ 0.5\bar{H}_m [\bar{A}_m(i) + \bar{A}_m(NB(m))] [b^v(i) + b^v(NB(m))] [X_n(N_i(j_2)) - X_n(N_i(j_1))] \right. \\ \left. + 0.25\bar{H}_m [\bar{A}_m(i) + \bar{A}_m(NB(m))] [b^u(i) + b^u(NB(m)) + a^v(i) + a^v(NB(m))] \right. \\ \left. \times [Y_n(N_i(j_1)) - Y_n(N_i(j_2))] \right\}. \end{aligned} \tag{A.25}$$

The  $G_x$  and  $G_y$  are given as

$$G_x = ADVU + VICX - \overline{ADVU} - \overline{VICX} \tag{A.26}$$

$$G_y = ADVV + VICY - \overline{ADVV} - \overline{VICY}, \tag{A.27}$$

where

$$\begin{aligned} \overline{ADVU} &= \iint \left[ \frac{\partial \bar{u}^2 D}{\partial x} + \frac{\partial \bar{u}\bar{v}D}{\partial y} \right] dx \, dy = \oint \bar{u}^2 D \, dy + \oint \bar{u}\bar{v}D \, dx \\ &= \sum_{m=1}^3 0.5 \{ [\overline{u^2(i)} + \overline{u^2(NB(m))}] \bar{D}_m [Y_n(N_i(j_1)) - Y_n(N_i(j_2))] \\ &\quad + [\overline{u(i)v(i)} + \overline{u(NB(m))v(NB(m))}] \bar{D}_m [X_n(N_i(j_2)) - X_n(N_i(j_1))] \}; \end{aligned} \tag{A.28}$$

$$\begin{aligned} \overline{ADVV} &= - \iint \left[ \frac{\partial \bar{u}\bar{v}D}{\partial x} + \frac{\partial \bar{v}^2 D}{\partial y} \right] dx \, dy = - \oint \bar{u}\bar{v}D \, dy - \oint \bar{v}^2 D \, dx \\ &= \sum_{m=1}^3 0.5 \{ [\overline{u(i)v(i)} + \overline{u(NB(m))v(NB(m))}] \bar{D}_m [Y_n(N_i(j_1)) - Y_n(N_i(j_2))] \\ &\quad + [\overline{v^2(i)} + \overline{v^2(NB(m))}] \bar{D}_m [X_n(N_i(j_2)) - X_n(N_i(j_1))] \}; \end{aligned} \tag{A.29}$$

$$\begin{aligned}
\overline{VISCX} &= \iint D\bar{F}_x dx dy \approx \iint \left[ \frac{\partial}{\partial x} \overline{2A_m H \frac{\partial u}{\partial x}} + \frac{\partial}{\partial y} \overline{A_m H \left( \frac{\partial u}{\partial y} + \frac{\partial v}{\partial x} \right)} \right] dx dy \\
&= \oint \left( \overline{2A_m H \frac{\partial u}{\partial x}} \right) dy - \oint \left[ \overline{A_m H \left( \frac{\partial u}{\partial y} + \frac{\partial v}{\partial x} \right)} \right] dx = 2 \oint H \left( \overline{A_m \frac{\partial u}{\partial x}} \right) dy - \oint H \left[ \overline{A_m \left( \frac{\partial u}{\partial y} + \frac{\partial v}{\partial x} \right)} \right] 2 dx; \quad (A.30)
\end{aligned}$$

and

$$\begin{aligned}
\overline{VISCY} &= \iint D\bar{F}_y dx dy \approx \iint \left[ \frac{\partial}{\partial y} \overline{2A_m H \frac{\partial v}{\partial y}} + \frac{\partial}{\partial x} \overline{A_m H \left( \frac{\partial u}{\partial y} + \frac{\partial v}{\partial x} \right)} \right] dx dy \\
&= -\oint \left( \overline{2A_m H \frac{\partial v}{\partial y}} \right) dx + \oint \left[ \overline{A_m H \left( \frac{\partial u}{\partial y} + \frac{\partial v}{\partial x} \right)} \right] dy \\
&= -2 \oint H \left( \overline{A_m \frac{\partial v}{\partial y}} \right) dx + \oint H \left[ \overline{A_m \left( \frac{\partial u}{\partial y} + \frac{\partial v}{\partial x} \right)} \right] dy. \quad (A.31)
\end{aligned}$$

Let us define

$$USH = \overline{A_m \frac{\partial u}{\partial x}}, \quad UVSH = \overline{A_m \left( \frac{\partial u}{\partial y} + \frac{\partial v}{\partial x} \right)}, \quad \text{and} \quad VSH = \overline{A_m \frac{\partial v}{\partial y}}, \quad (A.32)$$

where  $u$  and  $v$  are the  $x$  and  $y$  components of the velocity output from the 3D model. At each  $\sigma$  level in a triangle cell, they can be expressed as a linear function as

$$u_{i,k}(x', y') = u_{i,k}(0, 0) + a_{(i,k)}^u x' + b_{(i,k)}^u y', \quad v_{i,k}(x', y') = v_{i,k}(0, 0) + a_{(i,k)}^v x' + b_{(i,k)}^v y'. \quad (A.33)$$

Then at the triangle cell  $i$ , we have

$$USH(i) = \overline{A_m \frac{\partial u}{\partial x}} = \sum_{k=1}^{KB-1} A_m(k) a_{(i,k)}^u, \quad (A.34)$$

$$VSH(i) = \overline{A_m \frac{\partial v}{\partial y}} = \sum_{k=1}^{KB-1} A_m(k) b_{(i,k)}^v, \quad (A.35)$$

$$UVSH(i) = \overline{A_m \left( \frac{\partial u}{\partial y} + \frac{\partial v}{\partial x} \right)} = \sum_{k=1}^{KB-1} A_m(k) [a_{(i,k)}^u + b_{(i,k)}^v]. \quad (A.36)$$

Therefore,

$$\begin{aligned}
\overline{VISCX} &= 2 \oint H \left( \overline{A_m \frac{\partial u}{\partial x}} \right) dy - \oint H \left[ \overline{A_m \left( \frac{\partial u}{\partial y} + \frac{\partial v}{\partial x} \right)} \right] dx \\
&= \sum_{m=1}^3 \bar{H}_m [USH(i) + UVSH(NB(m))] [Y_n(N_i(j_1)) - Y_n(N_i(j_2))] \\
&\quad + 0.5 \sum_{m=1}^3 \bar{H}_m [UVSH(i) + UVSH(NB(m))] [X_n(N_i(j_2)) - X_n(N_i(j_1))]; \quad (A.37)
\end{aligned}$$

$$\begin{aligned}
\overline{VISCY} &= -2 \oint H \left( \overline{A_m \frac{\partial v}{\partial y}} \right) dx + \oint H \left[ \overline{A_m \left( \frac{\partial u}{\partial y} + \frac{\partial v}{\partial x} \right)} \right] 2 dy \\
&= \sum_{m=1}^3 \bar{H}_m [VSH(i) + VSH(NB(m))] [X_n(N_i(j_2)) - X_n(N_i(j_1))] \\
&\quad + 0.5 \sum_{m=1}^3 \bar{H}_m [UVSH(i) + UVSH(NB(m))] [Y_n(N_i(j_1)) - Y_n(N_i(j_2))]. \quad (A.38)
\end{aligned}$$

*b. The 3D internal mode*

The 3D momentum equations can be rewritten as

$$\frac{\partial uD}{\partial t} + R_u = \frac{1}{D} \frac{\partial}{\partial \sigma} \left( K_m \frac{\partial u}{\partial \sigma} \right), \quad \frac{\partial vD}{\partial t} + R_v = \frac{1}{D} \frac{\partial}{\partial \sigma} \left( K_m \frac{\partial v}{\partial \sigma} \right), \quad (\text{A.39})$$

where

$$R_u = ADVU3 + CORX3 + HVISCX + DPBPX3 + BPBCX3, \quad (\text{A.40})$$

$$R_v = ADVV3 + CORY3 + HVISCY + DPBPY3 + BPBCY3. \quad (\text{A.41})$$

The numerical integration is conducted in two steps. At the first step, the ‘‘transition’’ velocity is calculated using all the terms except the vertical diffusion term in the momentum equations. Then the true velocity is determined implicitly using a balance between the local change of the ‘‘transition’’ velocity and the vertical diffusion term.

Let  $u_{i,k}^*$  and  $v_{i,k}^*$  be the  $x$  and  $y$  components of the ‘‘transition’’ velocity at the midpoint between  $k$  and  $k + 1$   $\sigma$  levels in triangle cell  $i$ . They can be determined numerically as follows:

$$u_{i,k}^* = u_{i,k}^n - \frac{\Delta t_l}{\Omega_i \Delta \sigma D_i} R_{u,(i,k)}^n, \quad v_{i,k}^* = v_{i,k}^n - \frac{\Delta t_l}{\Omega_i \Delta \sigma D_i} R_{v,(i,k)}^n, \quad (\text{A.42})$$

where  $\Delta \sigma = \sigma_k - \sigma_{k+1}$ ,  $\Delta t_l$  is the time step for the internal mode.

Each term in  $R_{u,(i,k)}^n$  and  $R_{v,(i,k)}^n$  is computed as follows:

$$\begin{aligned} ADVU3_{(i,k)}^n &= \iint \left[ \int_{\sigma_{k+1}}^{\sigma_k} \left( \frac{\partial u^2 D}{\partial x} + \frac{\partial uvD}{\partial y} + \frac{\partial u\omega}{\partial \sigma} \right) d\sigma \right] dx dy \\ &= (\sigma_k - \sigma_{k+1}) \sum_{m=1}^3 u_{i,k}^n(m) \bar{D}_m v_{n,k}^n(m) \hat{l}_m + \Omega_i [(u_{i,k-1}^n + u_{i,k}^n) \omega_{i,k}^n - (u_{i,k}^n + u_{i,k+1}^n) \omega_{i,k+1}^n]; \end{aligned} \quad (\text{A.43})$$

$$\begin{aligned} ADVV3_{(i,k)}^n &= \iint \left[ \int_{\sigma_{k+1}}^{\sigma_k} \left( \frac{\partial uvD}{\partial x} + \frac{\partial v^2 D}{\partial y} + \frac{\partial v\omega}{\partial \sigma} \right) d\sigma \right] dx dy \\ &= (\sigma_k - \sigma_{k+1}) \sum_{m=1}^3 v_{i,k}^n(m) \bar{D}_m v_{n,k}^n(m) \hat{l}_m + \Omega_i [(v_{i,k-1}^n + v_{i,k}^n) \omega_{i,k}^n - (v_{i,k}^n + v_{i,k+1}^n) \omega_{i,k+1}^n]; \end{aligned} \quad (\text{A.44})$$

$$CORX3 = -fv_i \bar{D}_i (\sigma_k - \sigma_{k+1}) \Omega_i, \quad CORY3 = fu_i \bar{D}_i (\sigma_k - \sigma_{k+1}) \Omega_i; \quad (\text{A.45})$$

$$\begin{aligned} HVISCX_{(i,k)}^n &= \iint \left( \int_{\sigma}^0 DF_x d\sigma \right) dx dy \approx \iint \left\{ \int_{\sigma}^0 \frac{\partial}{\partial x} \left[ 2A_m H \frac{\partial u}{\partial x} \right] + \frac{\partial}{\partial y} \left[ A_m H \left( \frac{\partial u}{\partial y} + \frac{\partial v}{\partial x} \right) \right] d\sigma \right\} dx dy \\ &= \left[ 2 \oint A_m H \frac{\partial u}{\partial x} dy - \oint \bar{A}_m H \left( \frac{\partial u}{\partial y} + \frac{\partial v}{\partial x} \right) dx \right] (\sigma_k - \sigma_{k+1}) \\ &= \left\{ \sum_{m=1}^3 0.5 \bar{H}_m [A_m(i) + A_m(NB(m))] (a_{(i,k)}^u + a_{(NB(m),k)}^u) [Y_n(N_i(j_1)) - Y_n(N_i(j_2))] \right. \\ &\quad \left. + \sum_{m=1}^3 0.25 \bar{H}_m (b_{(i,k)}^u + b_{(NB(m),k)}^u + a_{(i,k)}^v + a_{(NB(m),k)}^v) [X_n(N_i(j_2)) - X_n(N_i(j_1))] \right. \\ &\quad \left. \times [A_m(i) + A_m(NB(m))] \right\} (\sigma_k - \sigma_{k+1}); \end{aligned} \quad (\text{A.46})$$

$$\begin{aligned}
HVISCY_{(i,k)}^n &= \iint \left( \int_{\sigma}^0 DF_y d\sigma \right) dx dy \approx \iint \left\{ \int_{\sigma}^0 \frac{\partial}{\partial y} \left[ 2A_m H \frac{\partial v}{\partial y} \right] + \frac{\partial}{\partial x} \left[ A_m H \left( \frac{\partial u}{\partial y} + \frac{\partial v}{\partial x} \right) \right] d\sigma \right\} dx dy \\
&= \left[ -2 \oint A_m H \frac{\partial v}{\partial y} dx + \oint \bar{A}_m H \left( \frac{\partial u}{\partial y} + \frac{\partial v}{\partial x} \right) dy \right] (\sigma_k - \sigma_{k+1}) \\
&= \left\{ \sum_{m=1}^3 0.5 \bar{H}_m [A_m(i) + A_m(NB(m))] (b_{(i,k)}^v + b_{(NB(m),k)}^v) [X_n(N_i(j_2)) - X_n(N_i(j_1))] \right. \\
&\quad \left. + \sum_{m=1}^3 0.25 \bar{H}_m (b_{(i,k)}^u + b_{(NB(m),k)}^u + a_{(i,k)}^v + a_{(NB(m),k)}^v) [Y_n(N_i(j_1)) - Y_n(N_i(j_2))] \right. \\
&\quad \left. \times [A_m(i) + A_m(NB(m))] \right\} (\sigma_k - \sigma_{k+1}); \tag{A.47}
\end{aligned}$$

$$DPBPX_{(i,k)}^n = g \bar{D}_i (\sigma_k - \sigma_{k+1}) \sum_{m=1}^3 \bar{\zeta}_m^n [Y_n(N_i(j_1)) - Y_n(N_i(j_2))]; \tag{A.48}$$

$$DPBPY_{(i,k)}^n = g \bar{D}_i (\sigma_k - \sigma_{k+1}) \sum_{m=1}^3 \bar{\zeta}_m^n [X_n(N_i(j_2)) - X_n(N_i(j_1))] \tag{A.49}$$

$$\begin{aligned}
PBCX3 &= -\frac{g}{\rho_o} \left\{ \iiint \int_{\sigma_{k+1}}^{\sigma_k} D \frac{\partial}{\partial x} \left[ D \left( \int_{\sigma}^0 \sigma \frac{\partial \rho}{\partial \sigma} d\sigma \right) \right] d\sigma dx dy + \iiint \int_{\sigma_{k+1}}^{\sigma_k} D^2 \frac{\partial \rho \sigma}{\partial x} d\sigma dx dy \right\} \\
&= -\frac{g}{\rho_o} \left\{ \bar{D}_i \oint \left( D \int_{\sigma}^0 \sigma \frac{\partial \rho}{\partial \sigma} d\sigma \right) dy + \bar{D}_i^2 \oint \rho \sigma dy \right\} [\sigma_k - \sigma_{k+1}]. \tag{A.50}
\end{aligned}$$

Let

$$PBC(i) = \int_{\sigma}^0 \sigma \frac{\partial \rho}{\partial \sigma} d\sigma = \sum_{k'=1}^k \sigma(k') [\rho(k') - \rho(k'+1)], \tag{A.51}$$

then

$$\begin{aligned}
DPBCX &= -\frac{0.5g}{\rho_o} (\sigma_k - \sigma_{k+1}) \left\{ \bar{D}_i \sum_{m=1}^3 \bar{D}_m [PBC(i) + PBC(NB_i(m))] [Y_n(N_i(j_1)) - Y_n(N_i(j_2))] \right. \\
&\quad \left. + \bar{D}_i^2 \sum_{m=1}^3 [\rho(i) + \rho(NB_i(m))] \sigma(k) [Y_n(N_i(j_1)) - Y_n(N_i(j_2))] \right\}. \tag{A.52}
\end{aligned}$$

Similarly, we can derive the y component of the baroclinic pressure gradient as

$$\begin{aligned}
DPBCY &= -\frac{0.5g}{\rho_o} (\sigma_k - \sigma_{k+1}) \left\{ \bar{D}_i \sum_{m=1}^3 \bar{D}_m [PBC(i) + PBC(NB_i(m))] [X_n(N_i(j_2)) - X_n(N_i(j_1))] \right. \\
&\quad \left. + \bar{D}_i^2 \sum_{m=1}^3 [\rho(i) + \rho(NB_i(m))] \sigma(k) [X_n(N_i(j_2)) - X_n(N_i(j_1))] \right\}. \tag{A.53}
\end{aligned}$$

The mathematic forms of the two equations in (A.39) are the same, so that they can be solved numerically using the same approach. The method used to numerically solve these equations was adopted directly from the ECOM-si (Blumberg 1994). For example, a detailed description of this method is given below for the  $u$  component of the momentum equation. The implicit discrete form of the first equation in (A.39) is given as

$$A_{i,k}u_{k+1}^{n+1} + B_{i,k}u_k^{n+1} + C_{i,k}u_{k-1}^{n+1} = u^*, \quad (\text{A.54})$$

where

$$A_{i,k} = -\frac{2K_m(k+1)\Delta t}{[D^{n+1}]^2(\sigma_k - \sigma_{k+1})(\sigma_k - \sigma_{k+1})}; \quad C_{i,k} = -\frac{2K_m(k)\Delta t}{[D^{n+1}]^2(\sigma_k - \sigma_{k+1})(\sigma_{k-1} - \sigma_{k+1})};$$

$$B_{i,k} = 1 - A_{i,k} - C_{i,k}. \quad (\text{A.55})$$

This is a tridiagonal equation and it ranges from  $k = 2$  to KB-2, where KB is the number of total  $\sigma$  levels in the vertical. The solution for  $u(k)$  is calculated by

$$u(k) = -\frac{A_{i,k}}{B_{i,k} + C_{i,k}VH(k-1)}u(k+1) + \frac{u^* - C_{i,k}VHP(k-1)}{B_{i,k} + C_{i,k}VH(k-1)}, \quad (\text{A.56})$$

where

$$VH(k) = -\frac{A_{i,k}}{B_{i,k} + C_{i,k}VH(k-1)}; \quad VHP(k) = \frac{u_{i,k}^* - C_{i,k}VHP(k-1)}{B_{i,k} + C_{i,k}VH(k-1)}. \quad (\text{A.57})$$

The equation for temperature or salinity as well as other passive tracers also can be rewritten as the form shown in (A.39), so they can be solved numerically using the exact same approach discussed above. The only difference is that  $\theta$  is calculated at nodes and has the same control volume as that used for  $\zeta$ . To shorten the text, we decide not to include the detailed description of the finite-volume numerical approach for tracer equations here.

#### REFERENCES

- Barth, T. J., 1993: Recent developments in high order K-exact reconstruction on unstructured meshes. AIAA Paper 93-0668.
- Bigham, G. N., 1973: Zone of influence-inner continental shelf of Georgia. *J. Sediment. Petrol.*, **43**, 207-214.
- Blanton, J. O., 1996: Reinforcement of gravitational circulation by wind. *Buoyancy Effects on Coastal and Estuarine Dynamics*. D. G. Aubrey and C. T. Friedrichs, Eds., Coastal and Estuarine Studies, 53, Amer. Geophys. Union, 47-58.
- Blumberg, A. F., 1994: A primer for Ecom-si. Tech. Rep., HydroQual, Inc., 66 pp.
- , and G. L. Mellor, 1987: A description of a three-dimensional coastal ocean circulation model. *Three-Dimensional Coastal Ocean Models*, N. S. Heaps, Ed., Coastal and Estuarine Series, Vol. 4, Amer. Geophys. Union, 1-16.
- Casulli, V., and R. T. Cheng, 1991: A semi-implicit finite-difference model for three-dimensional tidal circulation. *Proc. Second Int. Conf. on Estuarine and Coastal Modeling*, Tampa, FL, ASCE, 620-631.
- Chen, C., L. Z. Zheng, and J. O. Blanton, 1999: Physical processes controlling the formation, evolution, and perturbation of the low-salinity front in the inner shelf off the southeastern United States: A modeling study. *J. Geophys. Res.*, **104**, 1259-1288.
- , J. Zhu, E. Ralph, S. A. Green, J. W. Budd and F. Y. Zhang, 2001: Prognostic modeling studies of the Keweenaw Current in Lake Superior. Part I: Formation and evolution. *J. Phys. Oceanogr.*, **31**, 379-395.
- , R. C. Beardsley, P. J. S. Franks, and J. V. Keuren, 2002: Influences of the diurnally varying heat flux on stratification and residual circulation on Georges Bank. *J. Geophys. Res.*, in press.
- Cockburn, B., S. Hou, and C. W. Shu, 1990: TVB Runge-Kutta local projection discontinuous Galerkin finite element method for conservation laws. IV: The multidimensional case. *Math Comput.*, **54**, 545-581.
- Dick, E., 1994: Introduction to finite-volume techniques in computational fluid dynamics. *Computational Fluid Dynamics*, J. F. Wendt, Ed., Springer-Verlag, 271-297.
- Dunstan, W. M., and L. P. Atkinson, 1976: Sources of new nitrogen for the South Atlantic Bight. *Estuarine Processes*, Vol. 1, M. Wiley, Ed., Academic Press, 69-78.
- Galperin, B., L. H. Kantha, S. Hassid, and A. Rosati, 1988: A quasi-equilibrium turbulent energy model for geophysical flows. *J. Atmos. Sci.*, **45**, 55-62.
- Haidvogel, D., J. Wilkin, and R. Young, 1991: A semi-spectral primitive equation ocean circulation model using vertical sigma and orthogonal curvilinear horizontal coordinates. *J. Comput. Phys.*, **94**, 151-184.
- Hubbard, M. E., 1999: Multidimensional slope limiters for MUSCL-type finite volume schemes on unstructured grids. *J. Comput. Phys.*, **155**, 54-74.
- Kobayashi, M. H., J. M. C. Pereira, and J. C. F. Pereira, 1999: A conservative finite-volume second-order-accurate projection method on hybrid unstructured grids. *J. Comput. Phys.*, **150**, 40-45.
- Kraus, E. B., 1972: *Atmosphere-Ocean Interaction*. Clarendon Press, 275 pp.
- Lynch, D. R., and C. E. Naimie, 1993: The M<sub>2</sub> tide and its residual on the outer banks of the Gulf of Maine. *J. Phys. Oceanogr.*, **23**, 2222-2253.
- Maday, Y., and A. T. Patera, 1989: Spectral element methods for the incompressible Navier-Stokes equations. *State-of-the-Art Surveys on Computational Mechanics*, A. K. Noor, Ed., ASME, 71-143.
- Marshall, J., A. Adcroft, C. Hill, L. Perelman, and C. Heisey, 1997a: A finite-volume, incompressible Navier-Stokes model for studies of the ocean on parallel computers. *J. Geophys. Res.*, **102**, 5753-5766.
- , C. Hill, L. Perelman, and A. Adcroft, 1997b: Hydrostatic, quasi-hydrostatic and non-hydrostatic ocean modeling. *J. Geophys. Res.*, **102**, 5733-5752.
- Mellor, G. L., and T. Yamada, 1974: A hierarchy of turbulence closure models for planetary boundary layers. *J. Atmos. Sci.*, **31**, 1791-1806.
- , —, and —, 1982: Development of a turbulence closure model for geophysical fluid problem. *Rev. Geophys. Space Phys.*, **20**, 851-875.
- , and A. E. Blumberg, 1985: Modeling vertical and horizontal

- diffusivities with the sigma coordinate system. *Mon. Wea. Rev.*, **113**, 1379–1383.
- Naimie, C. E., 1996: Georges Bank residual circulation during weak and strong stratification periods: Prognostic numerical model results. *J. Geophys. Res.*, **101**, (C3), 6469–6486.
- Pomeroy, L. R., J. O. Blanton, G. A. Poffenhofer, K. L. V. Damm, P. G. Verity, H. L. Windom, and T. N. Lee, 1993: Inner shelf processes. *Ocean Processes: U.S. Southeast Continental Shelf*, D. W. Menzel, Ed., U.S. Dept. of Energy, 9–43.
- Reed, W. H., and T. R. Hill, 1973: Triangular and methods for the neutron transport equation. Tech. Rep. LA-UR-73-479, Los Alamos Scientific Laboratory.
- Simpson, J. J., and T. D. Dickey, 1981a: Alternative parameterizations of downward irradiance and their dynamical significance. *J. Phys. Oceanogr.*, **11**, 876–882.
- , and —, 1981b: The relationship between downward irradiance and upper ocean structure. *J. Phys. Oceanogr.*, **11**, 309–323.
- Verity, P. G., J. A. Yoder, S. S. Bishop, J. R. Nelson, D. B. Craven, J. O. Blanton, C. Y. Robertson, and C. R. Tronzo, 1993: Composition, productivity and nutrient chemistry of a coastal ocean planktonic food web. *Cont. Shelf Res.*, **13**, 741–776.
- Ward, M. C., 2000: An unsteady finite volume circulation model. *Estuarine and Coastal Modeling: Proceedings of the 6th International Conference, November 3–5, 1999, New Orleans, Louisiana*, M. L. Spaulding and H. L. Butler, Eds., ASCE, 17–33.
- Wu, L., and D. B. Bogy, 2000: Use of an upwind finite volume method to solve the air bearing problem of hard disk drives. *Comput. Mech.*, **26**, 592–600.
- Zheng, L., and C. Chen, 2000: A 3D modeling study of the estuarine system: An application to the Satilla River. *Estuaries and Coastal Modeling: Proceedings of the 6th International Conference, November 3–5, 1999, New Orleans, Louisiana*, M. L. Spaulding and H. L. Butler, Eds., ACSE, 1128–1149.
- , —, M. Alber, C. Alexander, and J. O. Blanton, 2002a: A 3-D modeling study of the Satilla River estuarine system. Part II: Suspended sedimentation. *Estuaries*, in press.
- , —, and J. Blanton, 2002b: A 3-D modeling study of the Satilla River estuarine system. Part I: Simulation of flooding/drying processes. *Estuaries*, in press.